NASA/TM—2017-219506

Axial-Flow Turbine Rotor Discharge-Flow Overexpansion and Limit-Loading Condition

Part 1: Computational Fluid Dynamics (CFD) Investigation

Shu-Cheng S. Chen
Glenn Research Center, Cleveland, Ohio

July 2017

NASA STI Program . . . in Profile

Since its founding, NASA has been dedicated to the advancement of aeronautics and space science. The NASA Scientific and Technical Information (STI) Program plays a key part in helping NASA maintain this important role.

The NASA STI Program operates under the auspices of the Agency Chief Information Officer. It collects, organizes, provides for archiving, and disseminates NASA's STI. The NASA STI Program provides access to the NASA Technical Report Server—Registered (NTRS Reg) and NASA Technical Report Server—Public (NTRS) thus providing one of the largest collections of aeronautical and space science STI in the world. Results are published in both non-NASA channels and by NASA in the NASA STI Report Series, which includes the following report types:

- TECHNICAL PUBLICATION. Reports of completed research or a major significant phase of research that present the results of NASA programs and include extensive data or theoretical analysis. Includes compilations of significant scientific and technical data and information deemed to be of continuing reference value. NASA counter-part of peer-reviewed formal professional papers, but has less stringent limitations on manuscript length and extent of graphic presentations.

- TECHNICAL MEMORANDUM. Scientific and technical findings that are preliminary or of specialized interest, e.g., "quick-release" reports, working papers, and bibliographies that contain minimal annotation. Does not contain extensive analysis.

- CONTRACTOR REPORT. Scientific and technical findings by NASA-sponsored contractors and grantees.

- CONFERENCE PUBLICATION. Collected papers from scientific and technical conferences, symposia, seminars, or other meetings sponsored or co-sponsored by NASA.

- SPECIAL PUBLICATION. Scientific, technical, or historical information from NASA programs, projects, and missions, often concerned with subjects having substantial public interest.

- TECHNICAL TRANSLATION. English-language translations of foreign scientific and technical material pertinent to NASA's mission.

For more information about the NASA STI program, see the following:

- Access the NASA STI program home page at http://www.sti.nasa.gov

- E-mail your question to help@sti.nasa.gov

- Fax your question to the NASA STI Information Desk at 757-864-6500

- Telephone the NASA STI Information Desk at 757-864-9658

- Write to:
  NASA STI Program
  Mail Stop 148
  NASA Langley Research Center
  Hampton, VA 23681-2199

NASA/TM—2017-219506

Axial-Flow Turbine Rotor Discharge-Flow Overexpansion and Limit-Loading Condition

Part 1: Computational Fluid Dynamics (CFD) Investigation

Shu-Cheng S. Chen
Glenn Research Center, Cleveland, Ohio

National Aeronautics and
Space Administration

Glenn Research Center
Cleveland, Ohio 44135

July 2017

This work was sponsored by the Advanced Air Vehicle Program
at the NASA Glenn Research Center

Level of Review: This material has been technically reviewed by technical management.

Available from

NASA STI Program
Mail Stop 148
NASA Langley Research Center
Hampton, VA 23681-2199

National Technical Information Service
5285 Port Royal Road
Springfield, VA 22161
703-605-6000

This report is available in electronic form at http://www.sti.nasa.gov/ and http://ntrs.nasa.gov/

Contents

Axial-Flow Turbine Rotor Discharge-Flow Overexpansion and Limit-Loading Condition
Part 1: Computational Fluid Dynamics (CFD) Investigation

Shu-Cheng S. Chen
National Aeronautics and Space Administration
Glenn Research Center
Cleveland, Ohio 44135

Summary

A computational fluid dynamics (CFD) investigation is conducted over a two-dimensional axial-flow turbine rotor blade row to study the phenomena of turbine rotor discharge-flow overexpansion at subcritical, critical, and supercritical conditions. The following quantitative data, averaged or integrated across the two-dimensional computational domain encompassing two blade passages, are obtained over a series of 14 inlet-total to exit-static pressure ratios, ranging from 1.5 (unchoked, subcritical condition) to 10.0 (excessively high-pressure ratio, supercritical condition):

- Mean-flow Mach numbers
- Mean-flow angles
- Axial component of mean-flow Mach number
- Tangential-blade surface-pressure forces
- Mean-flow mass flux
- Flow-path total-pressure-loss coefficients

Detailed flow features over the full domain of computation, such as the streamline patterns, Mach contours, pressure contours, blade surface pressure distributions, and so forth, are collected and presented in this paper. A formal, quantitative definition of the limit-loading condition based on the channel flow theory is proposed and explained.

Contrary to the comments made in the historical documentation on this subject about the deficiency of the theoretical methods applied in analyzing these phenomena, using the modern CFD method for the study of this subject appears to be successful. This paper describes the CFD study and its findings.

1.0 Introduction

The fact that axial-flow turbine vanes and blades of an aircraft engine can operate at the beyond-choked condition has been described and discussed as early as the 1950s. In a National Advisory Committee for Aeronautics (NACA) Research Memorandum (Ref. 1), experimental testing in a two-dimensional cascade wind tunnel on a row of axial-flow turbine rotor blades was conducted to study the phenomena of turbine rotor discharge-flow overexpansion at critical and supercritical conditions. The results were compared with five theoretical methods of analysis. This subject was also described schematically and analytically in Horlock (Ref. 2). From these two articles, it is understood that at the critical condition (the onset of blade choking) and beyond (the supercritical conditions) characteristic waves of both families are formed at the opposing corners of the blade-row trailing edge, where expansion waves were observed on one side of the blade surface and compression waves were formed on the opposite side of the blade end. The flow at the blade-row discharge is deflected, owing to the presence of these characteristic waves, by an angle dependent on the pressure ratio (PR) applied across the blade

row. The rotor blade surface-pressure force continues to increase in the supercritical flow regime until a plateau is reached where both the tangential discharge-flow velocity and the blade loading (the blade surface-pressure force) exhibit a constant trend.

However, a detailed picture, quantitative analysis, and understanding associated with these phenomena were absent. The comments and conclusions of the two reports (Refs. 1 and 2) stated that none of the analytical methods investigated had produced satisfactory results in comparison with the experimental findings, with little explanation of why or how they were different. The experimental data obtained were mostly about the discharge-flow angle deflections, while other quantitative data such as flow Mach number, velocity components, pressure field, tangential-blade surface-pressure force, and so forth, were unclear or absent.

In this paper, a computational fluid dynamics (CFD) investigation is conducted over the same experimental apparatus described in Reference 1 (but with a different turbine rotor blade shape). Quantitative data of the mean-flow Mach number, mean-flow angle, the tangential blade pressure force, the mean-flow mass flux, and the flow path total pressure loss coefficients, averaged or integrated across a two-dimensional computational domain encompassing two blade passages, are obtained over a series of 14 inlet-total to exit-static PRs, from 1.5 (unchoked; subcritical condition) to 10.0 (supercritical with excessively high PR). Detailed flow features over the full domain of computation, such as the streamline pattern, Mach contour, pressure contour, blade surface pressure distribution, and so forth, are collected and displayed. A formal, quantitative definition of the limit-loading condition based on the channel flow theory is proposed and explained.

Contrary to the comments made in References 1 and 2 about the deficiency of the theoretical methods applied in analyzing these phenomena, using the CFD method for the study of this subject appears to be successful. A head-to-head comparison with experimental data of the same apparatus and geometry is needed to form a definitive conclusion. This experimental comparison is unavailable at present.

This paper describes the CFD investigation and its findings.

Nomenclature

CFD	computational fluid dynamics
E^3	Energy Efficient Engine
HPT	high-pressure turbine
NACA	National Advisory Committee for Aeronautics
PR	pressure ratio
TVD	total variation diminishing

Symbols

A	cross section area normal to the flow
G	unit conversion factor needed for the system of U.S customary units
M	flow Mach number
M_x	axial component of mean-flow Mach number
$\bar{M}$	mean-flow Mach number
$\dot{m}$	mean-flow mass flux
P	static pressure
Pt	total pressure
p	blade surface static pressure
R	specific gas constant
T	static temperature
Tt	total temperature

u axial velocity
$\bar{u}$ mean-flow axial velocity
v tangential velocity
$\bar{v}$ mean-flow tangential velocity
x axial coordinate
ρ density
β flow angle
ω mass flow rate
γ specific heat ratio

2.0 Computational Fluid Dynamics (CFD) Method, Geometry, and Computation Arrangement

This section contains a brief description of the CFD code and the functionalities applied.

Commercial code ANSYS® CFX (version 15.0) was used for this work. The functionality applied are the standard (default) options in the package. Two-dimensional, steady-state, full Navier-Stokes equations for compressible flow were solved. The high-resolution scheme (the default scheme), which is equivalent to a second order upwind differencing scheme with total variation diminishing, was applied. The turbulence model equations were the standard K-epsilon (k-ε) turbulence model with scalable wall function, noted in the documentation of CFX. The ideal gas property of air was chosen. CFX used an unstructured grid with automatic mesh generation. Meshes in the vicinity of walls were compacted and stretched outward to better resolve the boundary-layer flow effect.

The blade geometry studied is a two-dimensional cross section of the GE Energy Efficient Engine (E^3) high-pressure turbine (HPT) near the rotor 1 hub (Ref. 3).

The computational domain encompassed two blade passages, with translational periodicity condition imposed on the top and bottom boundaries. The geometry and a two-dimensional mesh structure for the computation are shown in Figure 1.

Data were collected and processed (reduced) along the boundary contours, as well as along two interior lines (Figure 2).

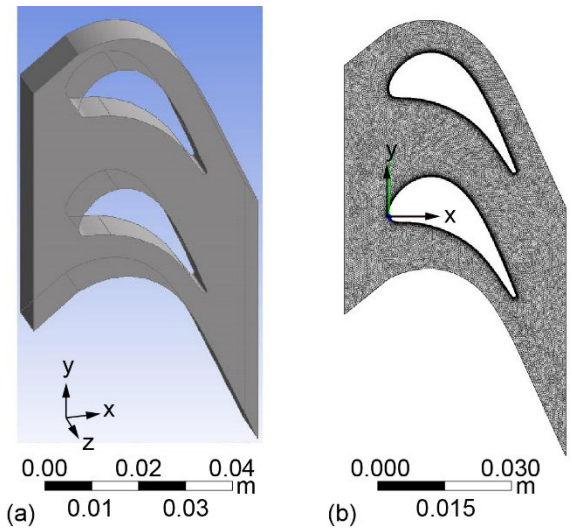

Figure 1.—Blade geometry and domain meshing (coarse mesh).

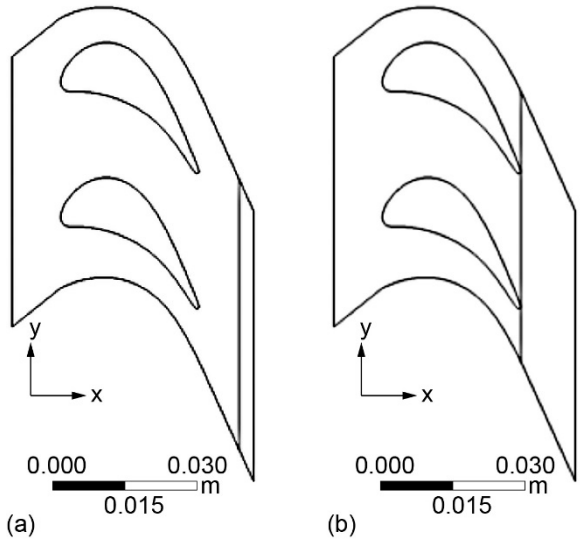

Figure 2.—Interior data collection lines. (a) Line 1. (b) Line 2.

TABLE I.—COMPUTATIONAL DOMAIN SPECIFICS

Description	Distance, m	Angle, deg
Inlet plane to discharge plane	0.050 (axial)	------
Inlet plane to blade leading edge	0.01014 (axial)	------
Blade leading edge to trailing edge	0.02832 (axial)	------
Blade trailing edge to exit plane	0.01154 (axial)	------
Blade to blade spacing	0.028 (tangential)	------
Line 1 to exit plane	0.00286 (axial)	------
Blade trailing edge to Line 2	0.000428 (axial)	------
Inlet blade/flow angle	----------	+38.6
Discharge blade angle	----------	–65.6

Mean flow quantities, such as mean-flow Mach number, mean-flow angle, mean-flow mass flux, the tangential-blade surface-pressure force, and the flow path total-pressure-loss coefficients, averaged or integrated over the designated contour lines or curves, were processed and obtained. Detailed flow pictures and solutions encompassing the entire computational domain, such as Mach lines, pressure contours, streamline patterns, and so forth, are collected and presented in Section 4.0.

Table I lists specifics about the computational domain.

The boundary conditions and the parametric matrix applied to the study are described in the following paragraphs.

The flow entered from the left and exited to the right. The inlet flow conditions applied are as follows:

- Total pressure (Pt_{in}) = 1.0 atm (1.01325×10^5 Pa)
- Total temperature Tt_{in} = 25 °C
- Flow angle (β_{in}) = +38.6°
- Turbulence intensity: medium

The exit flow condition enforced was the contour-averaged exit-static pressure along the line (plane) of exit. A parametric study of 14 total ratios was conducted, varying along a single flow parameter: the inlet-total to exit-static PR. The PR varied from an unchoked (subcritical) condition of PR = 1.5 to an excessively high (high supercritical) condition of PR = 10.0. The matrix of study for the PR is:

PR = 1.5, 1.75, 2.0, 2.25, 2.5, 2.75, 3.0, 3.25, 3.5, 4.0, 4.5, 5.0, 7.5, 10.0

The flow properties applied in this study should be understood as representing quantities of the relative (rotational) frame because the rotor is being studied. The total pressure, total temperature, flow velocities, flow angles, and Mach numbers in this study are referring to quantities in the relative frame of reference (with respect to a designated, constant speed of rotation). This is not to be misinterpreted as quantities of the absolute (stationary) frame. This computational rationale is the same as the rationale applied and executed in the experiment of Reference 1.

Solid wall (smooth) with no slip and adiabatic condition was applied to all blade surfaces. As previously mentioned, translational periodicity was imposed along the top and the bottom boundaries.

Gauge pressure was used in the computation instead of the absolute pressure. The figures presented in this paper that include pressure contours or pressure levels are based on gauge pressure.

3.0 Mesh Refinement and the Solution-Seeking Procedure

Three tiers of systematic mesh refinement were conducted. The mesh densities are shown in Table II.

TABLE II.—MESH DENSITY

Structures	Elements
Coarse	207,000
Fine	445,000
Finer	772,000

Flow solutions were first obtained on the coarse mesh iteratively and parametrically, then the mesh was refined and the process was repeated on the refined-mesh system, and so on. The initial guess of the flow field utilizes the existing flow solution obtained. Whenever applicable, the initialization used the solution obtained from the preceding ratio of the same mesh density, and continued parametrically from one PR to the next in sequence. This process proved to be the most stable and consistent one. A converged solution was obtained (conceived) in only a few tens of iterations (with a local Courant-Friedrichs-Lewy number of 0.5) for each ratio.

Convergence criteria specified were that the "residual" (of the default definition of ANSYS® CFX) of each governing equation of the system achieve the level of less than 1×10^{-4}. These criteria were observed as achievable to the momentum and the energy equations. The pressure variation (the equation linked to the mass conservation), however, was observed leveling off at 2×10^{-4} and was incapable of reducing further. This was observed in the denser mesh systems studied (the fine and the finer meshes) and was particularly noticeable in the finer mesh system. The turbulence modeling equations, k-ε, were surprisingly well behaved. For the most part, they converged nicely as that of the momentum and energy equations did. However, at high supercritical ratios, the turbulence dissipation equation also leveled off at a higher level comparable to that shown by the pressure equation.

This level of convergence is satisfactory for the engineering application of the present study. Small features, however, were contaminated by the residual of the solution and were accurate only to the level of convergence achieved by the stiffest equation of the system. This is observed in plots of Mach-line contours of the subcritical (PR = 1.5) ratio. This will be discussed at length in the next section.

4.0 Results and Discussion

Mean flow quantities, such as mean-flow Mach number, mean-flow angle, the axial component of mean-flow Mach number, averaged across the interior data collection Lines 1 and 2 (depicted in Figure 2), are presented and discussed. The tangential-blade surface-pressure forces (the blade loadings) integrated over the upper and the lower blade surfaces obtained parametrically throughout the study matrix are collected and presented in this section.

Detailed flow features and flow solutions encompassing the entire computational domain, such as the Mach lines, pressure contours, streamline patterns, and so forth, are presented and discussed.

4.1 Mean Flow Properties

A standalone Fortran code was written to generically read-in the XY type of data file exported from ANSYS® CFX, in plain text format. The flow Mach number (M), axial (u) and tangential (v) velocity components, static pressure (P), total pressure (Pt), and density (ρ) were exported from the module "CFD-post" and processed by averaging or integrating over the designated lines or contours.

Mean-flow Mach numbers ($\bar{M}$), mean-flow axial ($\bar{u}$) and tangential ($\bar{v}$) velocity components were obtained at the interior Lines 1 and 2 (Figure 2) by straightforward line averaging. The flow angle (β) was obtained as

$$\beta = \tan^{-1}\left(\overline{v}/\overline{u}\right) \tag{1}$$

The axial component of the mean-flow Mach number (M_x) was obtained as

$$M_x = \overline{M} * \cos(\beta) \tag{2}$$

This kind of data reduction is basic. Strictly speaking, (β) and (M_x) should be calculated as

$$\beta = \overline{\tan^{-1}\left(v/u\right)} \tag{3}$$

$$M_x = \overline{\mathrm{M} * \cos\left[\tan^{-1}\left(v/u\right)\right]} \tag{4}$$

However, Equations (3) and (4) would require processing of multiple input data files and the data reduction code would have to be more sophisticated. This level of sophistication is currently being implemented but was not available at the time when these quantities were processed. Therefore, Equations (1) and (2) are the data presented in this paper. Small discrepancies between the results of Equations (3) and (4) and that of Equations (1) and (2) can be expected however.

The mean-flow mass flux, $\dot{m}$, however, was calculated at Line 2 (immediately downstream of the rotor discharge station) with the advanced processing as

$$\dot{m} = \overline{\rho u} \tag{5}$$

The mean-flow total pressure at Lines 1 and 2 was obtained as

$$Pt_{\mathrm{line}} = \overline{Pt} \tag{6}$$

The total-pressure-loss coefficient was defined and calculated as

$$Pt_{\mathrm{loss}} = \left(Pt_{\mathrm{in}} - Pt_{\mathrm{line}}\right)/Pt_{\mathrm{in}} \tag{7}$$

The tangential-blade surface-pressure force was calculated as

$$P_{\mathrm{force}} = \left|\left\{\left|\int_1^2 p\,\mathrm{d}x\right| - \left|\int_2^1 p\,\mathrm{d}x\right|\right\}\right| \tag{8}$$

Where in Equation (8), the first integration was performed at the upper blade surface, from a leading edge point (pt. 1) to a trailing edge point (pt. 2); the second integration was conducted at the lower blade surface of another blade, from the trailing edge point to the leading edge point. Integration was performed over the axial coordinate (x).

Over the blade surface, the XY plot can be arranged to be a complete loop around a single blade, covering both the upper and lower surfaces of the blade in one piece. For this type of data file, the integration in Equation (8) would simply be a single loop-around integration. This variation in data format has been considered and is included in the data reduction code.

4.2 Mean Flow Properties Presentation

Mean-flow Mach number, mean-flow angle, and the axial component of the mean-flow Mach number obtained at interior data collection Lines 1 and 2 (Figure 2) and collected from the three tiers of mesh refinement of the parametric study are presented in this section. The data processed at Line 2 (immediately after the rotor discharge) are presented first in Figure 3, followed by the results obtained at Line 1 (further downstream of the rotor, see Table I for the perspective spacing) shown in Figure 4.

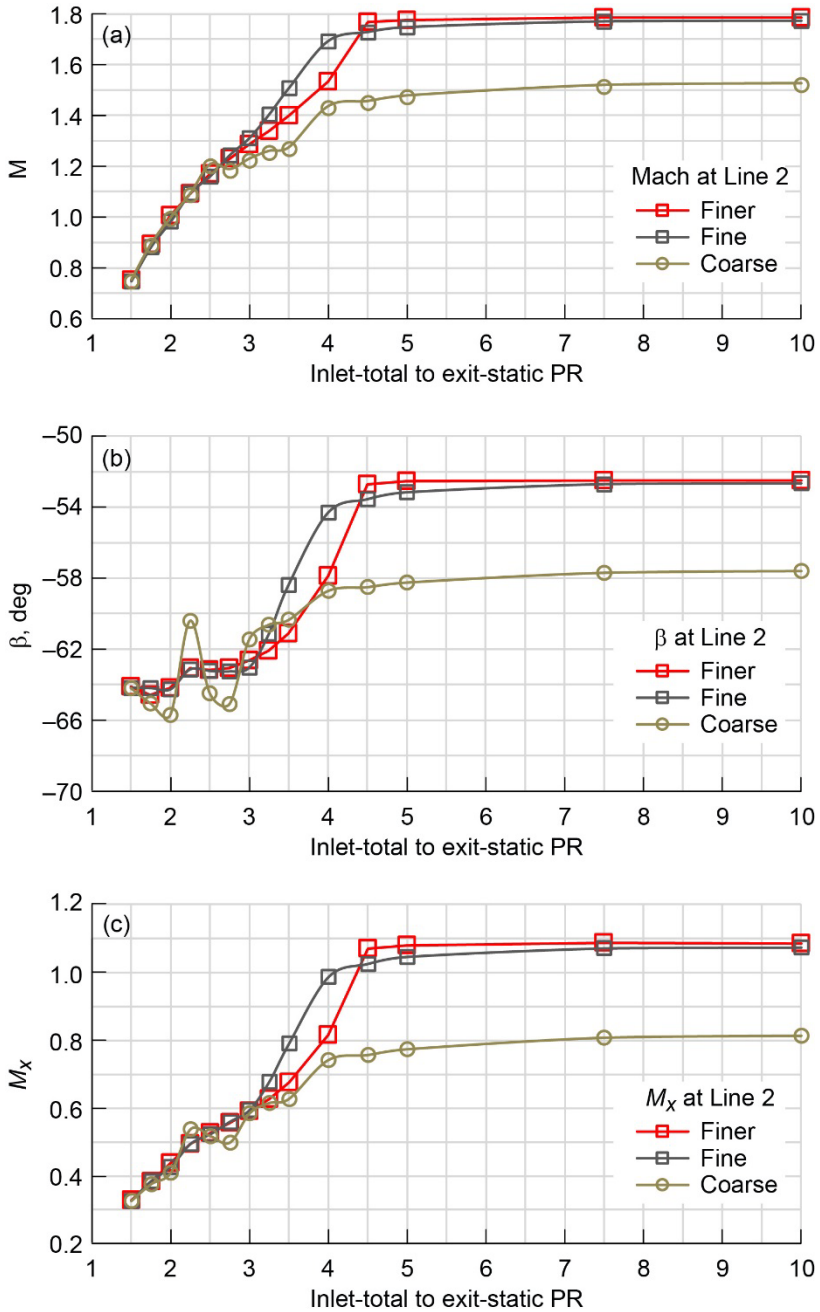

Figure 3.—Mesh-refinement results comparison at Line 2. (a) Mean-flow Mach number. (b) Mean-flow angle. (c) Axial component of mean-flow Mach number. PR, pressure ratio.

Some remarks with regard to the computational aspect of the results are noted first. These observations also apply to data collected and presented at Line 1, shown in Figure 4.

Through mesh refinement, clearly the solutions obtained are consolidating. The difference of the solution of the coarse mesh with respect to the solution of the fine mesh and that of the finer mesh is astounding. The coarse mesh result is grossly underpredicting and is oscillatory. The fine mesh result was decent in trending and magnitude, but diffusive in comparison to the finer mesh result. This result was

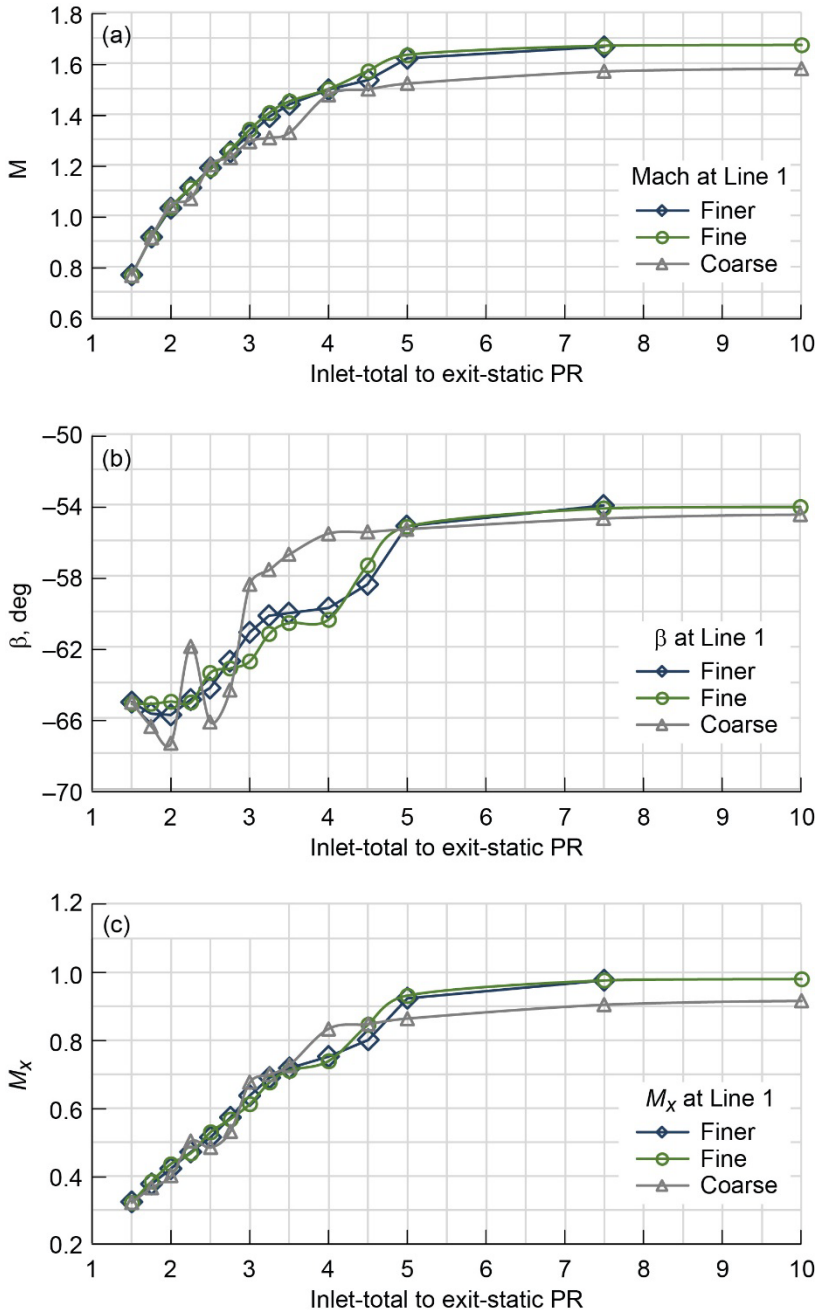

Figure 4.—Mesh-refinement results comparison at Line 1. (a) Mean-flow Mach number. (b) Mean-flow angle. (c) Axial component of mean-flow Mach number. PR, pressure ratio.

unexpected because the coarse mesh contained 207,000 elements (as shown in Table II), which is not a small number for a two-dimensional domain of a rather simple and straightforward geometry. The fine mesh system contained 445,000 elements, which is considered quite large, yet the result is diffusive in the supercritical flow regime (demarcation of the subcritical, critical, and supercritical flow regimes is defined later). The finer mesh result was satisfactory and regarded as the standard of this study. In order to achieve this solution, the number of elements applied (772,000) exceeded three-quarters of a million, which is unusually large. An explanation for this high demand of mesh resolution is that the flow investigated in this study is mostly in the high-pressure ratio flow regime and the flow Mach numbers are predominately transonic to supersonic. In the critical and supercritical flows of a turbine blade row, complex characteristic waves of both families (compression and expansion) resided in the latter part of the blade passages and beyond, which covered about half of the computational domain (the details of the flow pattern will be shown later in this section). The computational method applied to this study was a second-order upwind-differencing scheme with total variation diminishing (TVD), which means that it degenerated automatically to a first-order scheme at the vicinity of a sharp gradient (a jump). Because the latter part of the flow domain is blanked with characteristic waves of considerably large (non smooth) flow-quantity variations across, the latter part of the flow domain was essentially solved by a first-order algorithm, which is known to be quite diffusive. Very high mesh resolution was needed to properly resolve the essential flow features, as the results shown here indicate.

Despite the high demand of grid resolution, the consolidated solution of the finer-mesh system appears to have captured the salient features of the phenomena described in Reference 1 and is regarded as the standard in this study.

The important physical features shown by the solution are noted here. The observation is focused on the finer mesh results. To better describe these features, the flow regimes and their corresponding PRs are defined as

- Subcritical flow condition/regime: PR < 2.25
- Critical flow condition: PR = 2.25
- Supercritical flow condition/regime: PR > 2.25

The demarcation is PR equals 2.25 for the study made in this work. This point represented the onset of choke of the flow in blade passage. Below PR = 2.25, the flow was unchoked throughout the flow path (subcritical) and above PR = 2.25, the flow was choked at the throat of the blade passage and was in the state of overexpansion at the blade-row discharge (supercritical). Detailed flow patterns encompassing the entire flow regimes will be shown graphically later in this section, which will clearly demonstrate the flow features described here.

Shown in Figure 3 immediately downstream from the rotor discharge, the mean-flow Mach number went from subsonic (~0.7) to supersonic (~1.8) with respect to the variation of the PR applied. The change was smoothly curving with curve inflection at the low to medium PRs, but merged into a straight-line constant at PR = 4.5 and beyond. The transition from smooth variation to constancy was abrupt. This trend is also observable in plots of the mean-flow angle and the axial mean-flow Mach number. The mean-flow angle exhibits deflection of about 12° total, from approximately –64° at subcritical conditions (with the discharge blade angle of –65.6°, given in Table I) to approximately –52° at constancy. The axial component of the mean-flow Mach number reached the value of 1.0 (1.07 to be precise, in the present study) when transitioning into the constant trend.

Further downstream at Line 1, the trends of the mean flow properties shown in Figure 4 are similar to the trends obtained at Line 2 (immediately downstream from the rotor discharge). However, the intensity

of the flow quantities is dissipating and diffusing noticeably. The magnitude of the flow Mach number is less than that obtained at Line 2, the flow angle deflection is smaller, and the axial component of the mean-flow Mach number did not reach the value of 1.0. The flow properties are continuously increasing with respect to the increase of PRs. Although the variation in flow quantities slowed down and showed signs of saturation in the higher PR flow regime, no abrupt transitioning was observed in the trending and no constant trend was established over the length of the matrix applied in the study.

The pattern (trending) of the mean-flow angle deflection observed at Line 2 (Figure 3) is consistent with that depicted graphically in Reference 1. The other distinct pattern noted in Reference 1 is the tangential blade loading (or the tangential discharge-flow velocity, the two are in fact one-to-one corresponding), which exhibited smooth saturation at higher operating PRs into a constant trend. This pattern is also clearly observable from the result of the CFD investigation and will be shown in the next section. The onset point of this constant trending (of the operating PR) is referred to as the "limit-loading condition." The constancy of the tangential-blade surface-pressure force is termed the "limit load" in this work. They will be identified quantitatively.

The tangential-blade surface-pressure force obtained from this study is presented in the next section.

4.3 Tangential-Blade Surface-Pressure Force

The tangential-blade surface-pressure force was processed and obtained through Equation (8). The results of the parametric study on 14 inlet-total to exit-static PRs over the three tiers of mesh refinement are collected and presented in Figure 5. Figure A.1 shows detailed plots of the blade surface static pressure distribution (of the finer mesh system) are presented in Appendix A.

The tangential-blade surface-pressure force (or the tangential blade loading; although the two are not identical, as the blade loading should also include contribution from the tangential component of the net viscous force exerted on the blade surface; however, as a practical matter the latter is nearly a constant with respect to the PR variation, and is fairly weak compared to the former; thus is considered negligible) increases smoothly with respect to the increase of PRs. There is no observable point of inflection on the curve. The changes were considerable at the lower PR regime, but slowed down at higher PRs and saturating (transitioned gradually) into a constant (at a magnitude of 1125 N/m). The onset of the constant trending was observed (conceived) to be at PR = 4.5. However, the constancy was fully established at a PR greater than 4.5 (e.g., at points of PR = 5.0, 7.5, 10.0). These descriptions are readily observable when viewed together with plots of the blade surface static pressure distribution shown in Appendix A. The onset point of establishment (PR = 4.5) of the constant trend noted here on the blade loading is also clearly distinguishable in plots of the mean flow properties at Line 2 (Figure 3).

For this study, the onset of the limit-loading condition was at inlet-total to exit-static PR of 4.5. The limit load (of the two-dimensional blade cross section) obtained was 1125 N/m. At beyond PR = 4.5, both the blade loading (or the rotor discharge tangential flow velocity) and the mean-flow angle deflection exhibited constancy and stopped changing despite the increased operating PR applied to the turbine blade row.

These observations and conclusions are consistent with that noted in the work of Reference 1. It is also noted here that while the experimental data of Reference 1 had not extended deep into the flow regime beyond the limit-loading condition, investigation of the current CFD work did.

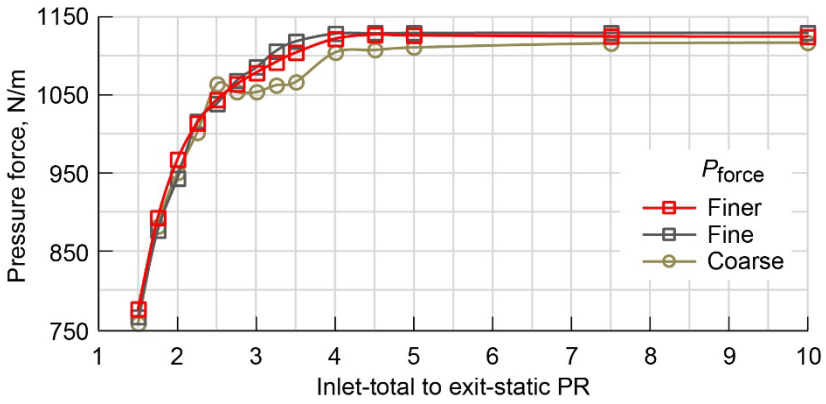

Figure 5.—Tangential-blade surface-pressure force. PR, pressure ratio.

4.4 Flow Features and Flow Patterns

The detailed flow solution and the flow patterns are shown here for better visualization of the phenomena described. Four representative ratios are presented here:

- PR = 1.5 (subcritical, unchoked)
- PR = 2.25 (critical, onset of blade choking)
- PR = 4.5 (supercritical, onset of limit-loading condition)
- PR = 10.0 (high supercritical, excessive PR)

Figure B.1 to Figure B.10 illustrate the remaining 10 ratios of flow solution, obtained at the other PR conditions, are displayed in Appendix B for reference.

4.4.1 Subcritical Flow

At an operating PR of subcritical, the flow is unchoked throughout the flow path. The lowest PR study in this work is PR = 1.5. The Mach-line contour, streamline pattern, static pressure distribution, and a composite plot of pressure with Mach-line contour imposed are shown in Figure 6.

Some observations for the subcritical flows are detailed in the following paragraphs.

The flow was unchoked and the Mach number was supersonic only locally with a very small bubble on the suction side of the blade surface. The streamlines were not deflected from the characteristic waves (they existed, but were weak and spotty). The discharge-flow angle deviation (due to the well-known Kutta condition), which was of major concern and required a considerable amount of modeling in the compressor flow (a retarding flow system), was insignificant for the turbine flow (an accelerating flow system). No more than 2° of flow angle deviation, with respect to the discharge blade angle, was observed for all the subcritical flows in this study. This result is shown in the plot of the mean-flow angle shown in Figure 3 (at PR = 1.5, 1.75, and 2.0).

The Mach-line contours highlighted in Figure 3 (Mach = 0.8 and 1.0) are broken and asymmetric to the periodicity condition. This is because these Mach lines are in fact small features to the bulk of flow quantities that reside in the field and they are contaminated by the residue of the pressure variation of the computational algorithm applied, which is at the level of 2×10^{-4} noted in Section 3.0. This contamination

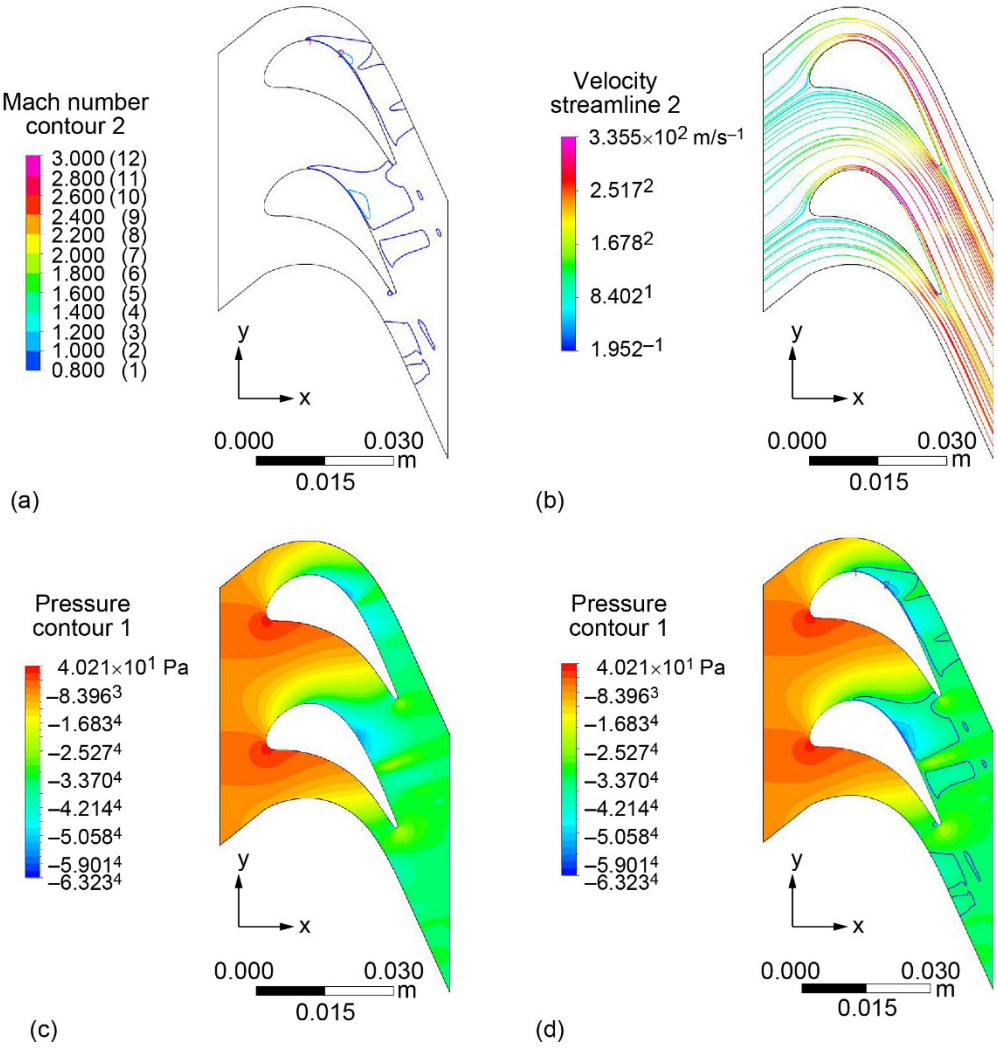

Figure 6.—Flow pattern and streamline contour unchoked (pressure ratio (PR) = 1.5). (a) Mach contour. (b) Streamlines. (c) Pressure contour. (d) Pressure with Mach contour imposed.

could not be removed by running the ratio with more iterations because this residue had already leveled off. Increasing the number of computational cells did not resolve the contamination either. This issue with small features was also observed in the fine-mesh system and it persisted in the finer-mesh system with refinement to an impeccably high mesh density, which indicates the issue is not because of insufficient grid resolution. If small features such as those shown are important, then changing the numerical integration method to improve the level of convergence achievable with a sufficient fine-mesh concentration would be necessary and could resolve this small feature problem. This issue of small feature contamination, however, is not noticeable in the higher PRs studied, because the small feature of this ratio (Mach-line contour of 0.8 and 1.0) is not particularly small to the higher PR flow solutions. For an engineering application such as the present study, the focus of discussion is on the bulk or measurable flow features. This issue of small feature contamination due to the insufficient level of convergence noted here was deemed nonessential to this study.

4.4.2 Critical Flow

Critical flow condition for this study was PR = 2.25. The mean flow properties of the coarse-mesh system showed a high elevation of oscillation at this condition, particularly noticeable in plots of the mean-flow angles (Figure 3 and Figure 4). Clearly, this is largely a false response of the numerical nature. In fine- and finer-mesh systems, this oscillatory behavior diminished greatly in magnitude (Figure 3 and Figure 4). Still, at this condition, the flow pattern is unusual and it is a major demarcation from the physical and mathematical flow regimes. For this study, critical condition is defined as the point at which the flow choking at the throat of the blade passage is barely established. The detailed flow picture and pattern are shown in Figure 7.

The sonic line is clearly visible in the Mach contour plot (the second line from the left, Figure 7(a)). Expansion waves are visible at the latter portion of the blade surface (along the suction side of the blade, Figure 7 (c)). A feathery-like structure appears in the Mach contour plot (Figure 7 (a)) and the flow at discharge is noticeably deflected at the trailing edge of the blade. However, this deflection is noticeable

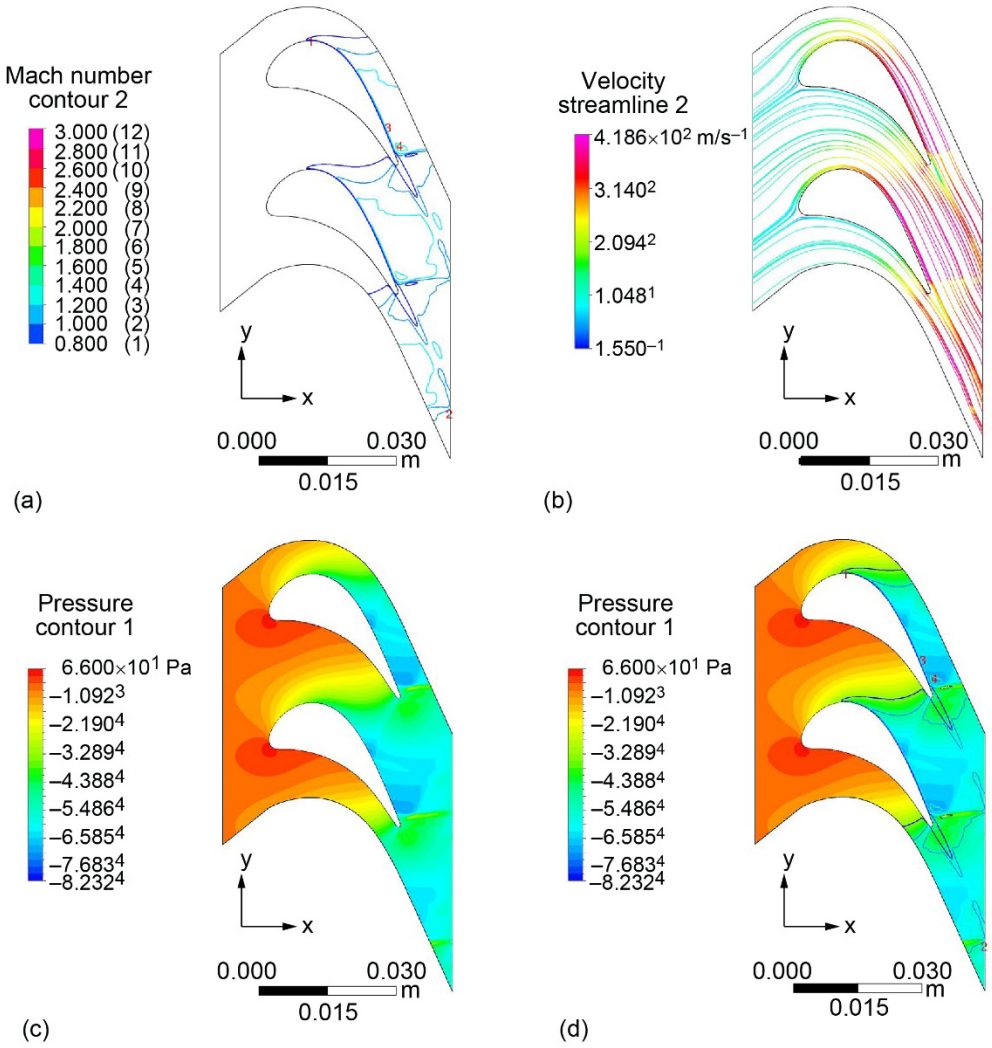

Figure 7.—Flow pattern and streamline contour at the onset of choke (pressure ratio (PR) = 2.25). (a) Mach contour. (b) Streamlines. (c) Pressure contour. (d) Pressure with Mach contour imposed.

only at a narrow region centering the blade's trailing edge and it is not noticeable in the majority portion of the discharge-flow area. From Figure 3, the plot of the mean-flow angle at Line 2 and the flow angle deflection (due to presence of the characteristic waves) shows an increase, but only about 1° more with respect to that of the subcritical flows for PRs up to 2.75 (at PR = 2.25, 2.5, 2.75). This indicates that the characteristic waves are fairly weak and still developing at the early stage of the critical-to-supercritical flow regime. Although the flow deflection at the blade trailing edge point is noticeable, the mean-flow angle is barely affected by the characteristic waves in the early stage of the supercritical flow conditions. This observation is also consistent with the description noted in Reference 1, which states that the flow deflection is observable at or even before the critical condition is established. What was not clarified in Reference 1 is that the observation was focused on the immediate vicinity of the blade-row trailing edge, and was not conducted in the mean sense, which averages across the entire plane of blade-row discharge.

4.4.3 Onset of Limit Load at Supercritical Flow Condition

The onset of the limit-loading condition for this study was PR = 4.5. The flow pattern at this condition is most interesting. The plots of the detailed flow features are shown in Figure 8.

The flow in the rotor passage is fully expanded. Flow at discharge is entirely supersonic, except for inside of the viscous layer, which is visible from the plots in Figure 8. An oblique shock wave emitting from the blade-row discharge off of the pressure-side corner can clearly be seen from both the Mach contour plot (Figure 8(a)) and the pressure contour (Figure 8(c)). This oblique shock wave was generated from the reflection of the expansion waves emitted from the latter portion of the suction surface of the blade. These expansion waves actually originated from the end corner of the pressure side of the blade surface and bounced back from the suction side of the blade surface toward the pressure side of the blade (while keeping the characteristics of an expansion wave; i.e., no sign change in the characteristics), hit the freestream flow off the pressure-side of the blade-row discharge, and then reflected back once more as compression waves (with a sign change in characteristics). The compression waves coalesced into an oblique shock wave (weak shock) due to the variation in the reflection angle of each wave that was impinged. The shock wave was curved and bulged into the flow domain beyond the blade-row discharge station. This flow picture was depicted and schematically illustrated in References 1 and 2, but not with the detail that is shown here (Figure 8). The expansion waves on the suction side of the blade surface appeared to end before the blade-row discharge, but beyond that point the expansion waves that were impinged skipped off and reflected back from the viscous boundary layer along the suction surface of the blade-end again as compression waves with a sign change. These compression waves (at the suction side of the blade end) congeal near the end corner of the suction surface and again formed another oblique shock wave with apparently stronger intensity than the oblique shock wave that was observed off of the pressure-side corner. This shock wave formation, on the other hand, was depicted prominently in References 1 and 2. The two oblique shock waves (one off of the pressure-side corner and the other off of the suction surface near the discharge station) were bracketing a quiescent zone, and the viscous layer (the wake) at the blade-row discharge stretched and settled between them (not as a shock wave, but as an entropy wave/gradient). This is not directly visible from the pressure contour plot (Figure 8), but it is clearly visible from the entropy contour plot and also visible in Mach-line contours with a clear and measurable amount of angle deflection at the close proximity of the blade-row trailing edge. The mean-flow angle is also clearly deflected by a substantial amount (about 12° with respect to the flow angle observed at the subcritical flow conditions) and this can be seen from the streamline plot here as well as from the plot of the mean-flow angle shown in Figure 3.

The flow quantities such as pressure, temperature, velocity, Mach number, flow angle, and so on, from the blade-row inlet to the blade-row discharge are almost completely developed at this condition

(the onset of the limit-loading condition, PR = 4.5). Virtually no further changes of the flow property in blade passages (upstream to the blade-row discharge station) will occur beyond this operating PR. In the flow domain after the blade-row discharge station, however, the flow properties still changed continuously with respect to the increased PR applied (or equivalently, with respect to the lowering of the backpressure at the domain exit). However, the amount of change was very modest and slow (referring to the mean flow properties here). This is displayed in Figure 4 and mentioned previously in Section 4.2. The detailed flow features, however, vary at a more noticeable pace, but the changes are mostly in the nature of stretching, redistribution, and local concentration. This flow picture will be further explored and discussed in the next section.

All the flow patterns and features described in this section are very interesting because they are highly nonlinear and interact with one another. As noted in References 1 and 2, no theoretical or analytical methods investigated in that era (the 1950s) were satisfactory in describing this overexpansion process. This is not surprising because the flow phenomena involved here are actually quite complex and highly

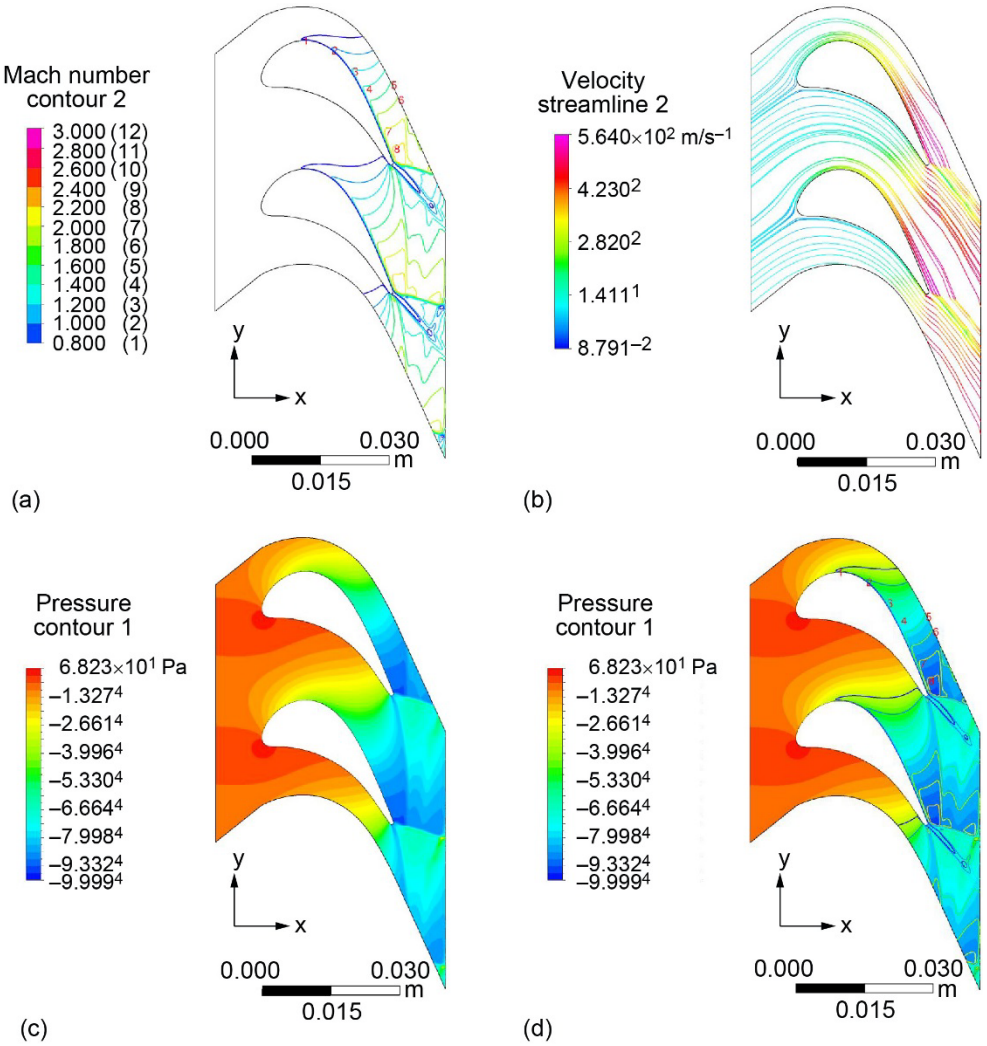

Figure 8.—Flow pattern and streamline contour at the onset of limit load (pressure ratio (PR) = 4.5). (a) Mach contour. (b) Streamlines. (c) Pressure contour. (d) Pressure with Mach contour imposed.

interactive. The CFD method, which tackles the full set of nonlinear Navier-Stokes equations simultaneously, appears to have the capacity to capture the physics of this overexpansion phenomena correctly and entirely.

There are many other noteworthy flow features and patterns, but they are not mentioned specifically here. The plots provided in the figures depict many of these flow features and patterns.

4.4.4 High Supercritical Flow With Excessive Pressure Ratio (PR)

An operating PR of 10.0 was calculated. The line-averaged static pressure at the outflow boundary was 1.47 psia (1/10 of 1 atmospheric pressure) for the exit-flow boundary condition, which is very low. The computation was processed and presented a converged solution. The solution is a legitimate numerical solution, but physically this exit boundary condition should be imposed further downstream from the blade-row discharge. The numerical contamination that is shown in Figure 9 will be discussed. The obtained flow patterns and features are displayed in Figure 9.

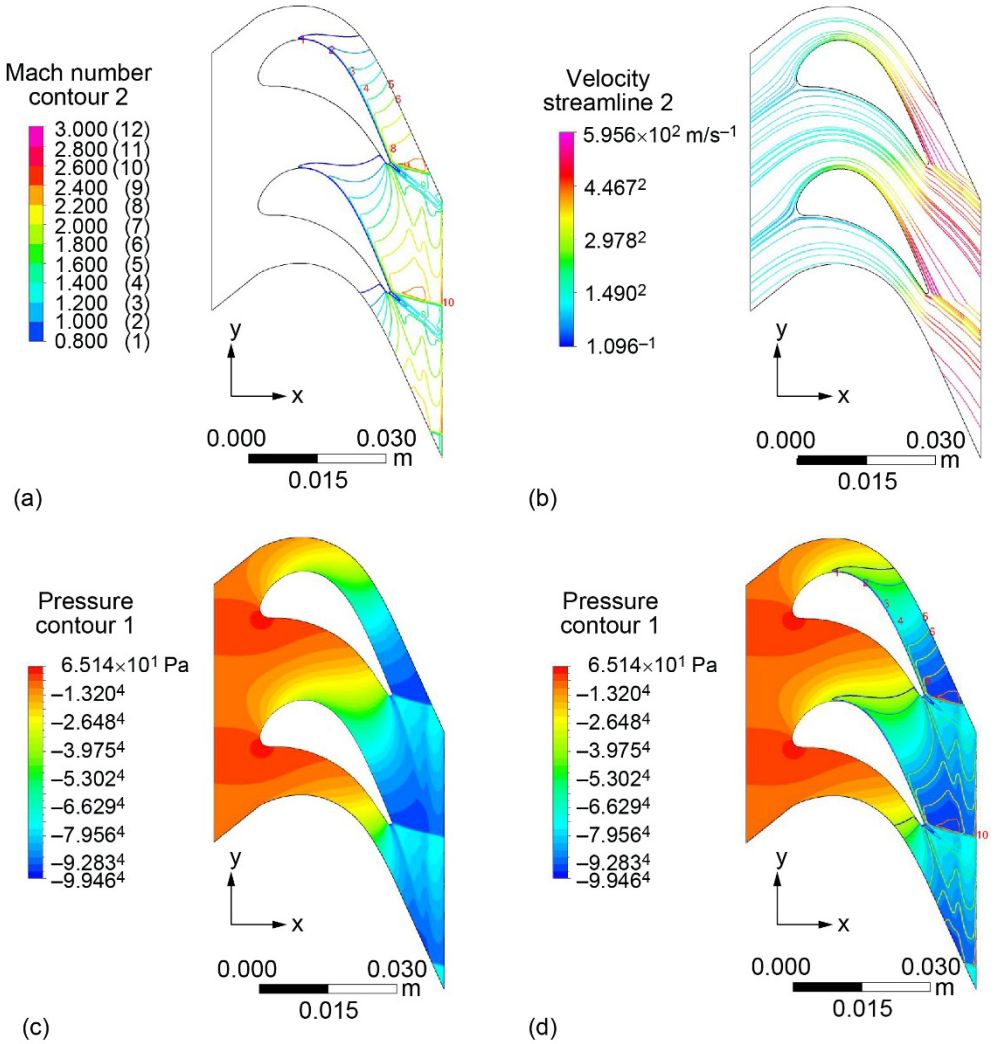

Figure 9.—Flow pattern and streamline contour at excessive pressure ratio (PR) = 10.0, where the outflow boundary is too close. (a) Mach contour. (b) Streamlines. (c) Pressure contour. (d) Pressure versus Mach contour imposed.

At the high supercritical flow condition, the streamline deflections were more uniformly across and looked pronounced at downstream, however, the amount of mean-flow angle deflection at the blade-row discharge station (at Line 2) remained exactly the same as those obtained when the limit loading was fully established (PR = 5.0, for example). This is seen from the mean-flow angle plot in Figure 3. The Mach-line contours within the blade-row passage remained nearly identical to that shown at onset of the limit load (PR = 4.5 in Figure 8). If compared with the plots of PR = 5.0 (Figure B.9), it could be concluded that they look exactly the same. The oblique shock wave off of the pressure-side corner (the weaker shock wave), however, bulges noticeably further downstream, compared to that shown in Figure 8. A high Mach number zone was formed downstream from the blade row off of the suction side of the blade surface, adjacent to the stronger oblique shock wave. The flow Mach number in that zone exceeded Mach 2.4. This high Mach number zone was not seen at the previous condition of PR = 4.5 (Figure 8).

In fact, all flow features beyond the blade-row discharge station evolved and are stretching out in the flow domain downstream to the blade-row discharge, seen clearly from the Mach contour and the pressure contour plots. These pictures seem to indicate a much different flow feature from PR = 4.5 to PR = 10.0, but the mean flow properties at Line 1 (near the exit plane, shown in Figure 4) indicated that the changes from the onset of the limit load (PR = 4.5) to PR = 10.0 are modest and slow. Actually, the mean-flow Mach number at the immediate downstream of the rotor (at Line 2) was 1.8 (Figure 3), whereas the mean-flow Mach number at near the domain exit (at Line 1) was less than 1.7 (Figure 4) at PR = 10.0, which suggests that the changes are more likely due to local stretching, diffusion, and redistribution rather than further expansion or acceleration.

It is important to note that although the flow at downstream to the blade-row discharge is still continuously evolving, all time-mean flow properties at and upstream of the blade-row discharge station remain exactly the same after limit loading is fully established (at PR = 5.0, 7.5, and 10.0). This can be seen quantitatively from plots of the mean flow properties shown in Figure 3 and qualitatively from the detailed contour plots shown here and in Appendix B.

Flow contamination due to the outflow boundary being too close to the blades can be seen clearly through the pressure contour plot in Figure 9(c). At the location near the exit boundary, enclosing the location of Line 1 (overlay Figure 2(a) and Figure 9(d)) where the mean flow data was acquired and processed there is a line of wavelets in Figure 9(d). These wavelets were caused by contamination of the outflow boundary condition, which has an exceedingly low static pressure at PR = 10.0. The expansion waves were deformed in the region close to the exit boundary after interacting with and passing through the oblique shock wave because the outflow boundary condition imposed was an artificial jump condition to the flow in the interior domain and the wavelet structure was formed as a result.

Data of the mean flow property of PR = 10.0 at Line 1 of the finer-mesh system was not included in the plots of Figure 4 because of the presence of this wavelet structure, which contaminated the finer-mesh solution at Line 1. This contamination was not as pronounced (severe) in the coarse- or fine-mesh system.

5.0 Limit-Loading Condition Hypothesis

The previous section paints a clear picture in regard to the phenomena of choked-flow overexpansion and the presence of a limit to the expansion process (the limit-loading condition). This section provides an explanation of how and why this limit exists. And also, to provide additional CFD findings, namely the quantitative behavior of the mean-flow mass flux before and after the onset of flow choking, and the flow path total-pressure-loss coefficients in associated with the axial turbine flows.

An axial-flow turbine blade passage, for either a stator or rotor, is basically a staggered, channel-flow passage. The flow, whether subcritical, critical, or supercritical, contained by and discharged from the

blade row follows the laws of physics and the rules of channel-flow analysis. From critical to supercritical conditions, two-family (of both the expansion and the compression) characteristic wave structures formed at the blade-row discharge (the channel outlet). The presence of waves for both families restricted the expansion process to be more constrained than that of the single-family wave expansion, in the sense that the compression waves were counter-balancing the expansion waves and the resulting flow Mach numbers and the flow expansion angles were limited in range. This is a general description of the channel-flow expansion phenomena. This subject is thoroughly explored and analyzed in textbooks of the compressible flows, for example, Shapiro (Ref. 4).

What the textbooks do not thoroughly cover is how and why a limit of the expansion process (the limit-loading condition) came about and that beyond a certain operating condition the expansion process would stop abruptly. The following paragraphs attempt to answer these questions. The content and the arguments made in this paper are more hypothetical than definitive in nature.

At a channel-flow outlet, a time- or ensemble-averaged discharge flow has an effective flow area. This effective flow area is defined as the geometric area of the channel outlet after subtracting the displacement thickness of the viscous layers present at that location. The derivative by length of this effective flow area normal to the outlet cross section would be zero at or at near the channel outlet. The mean-flow Mach number at the zero derivative of the effective cross section area is then a critical point, which indicates that the mean-flow Mach number also would have a derivative by length of zero at that point. This is a natural physical condition that exists at any geometric channel outlet.

At a certain operating condition, for example, at the operating PR of the limit-loading condition described and specified in the previous section of this paper, the discharge-flow Mach number would reach its maximum critical value at the channel outlet. At a high enough PR, the mean-flow Mach number at the channel outlet would have reached its peak value and not exceed it even if imposed with a higher operating PR. The mean-flow Mach number at lower operating PRs is critical, meaning the derivative of it with respect to the normal distance to the channel outlet is zero, but the value is below the extrema. The transition from below the extrema to the extrema and remaining constant thereafter is abrupt with respect to the imposed operating PRs, as indicated by Figure 3. This trend of behavior was unexpected.

The value of extrema of the mean-flow Mach number is dependent on the area expansion ratio of the physical geometry defined by the channel (the blade passage). For a geometrically convergent or constant area blade passage with respect to the direction normal to the channel outlet, this extremum equals 1.0 for the component of the mean-flow Mach number normal to the channel-outlet cross section (e.g., the axial component of the mean-flow Mach number presented in this work, because the blade-row outlet of an axial-flow turbine is normal to the axial direction). For a geometrically divergent channel (blade passage), this extremum could be higher than 1.0 if this geometric area expansion ratio is higher than 1.0 at the blade-row discharge. This analysis is generic and valid for all channel-flow physics, although it has not been applied and discussed specifically to the study of an axial-flow turbine blade row. The theoretical basis of this is included in Shapiro (Ref. 4), but because it is all encompassing, the mathematics of it is general and were not specific to this study. The same argument presented here was also hinted at in References 1 and 2, but not with the same clarity.

The axial component of the mean-flow Mach number at the rotor discharge (at Line 2) of this study has an extremum of about 1.07, as indicated in Figure 3. This suggests that the rotor blade-row geometry is slightly divergent with respect to the direction normal to the outlet plane of the blade row at the end portion of the blade passage. Had it been a convergent or constant area discharge blade passage, as the one tested in the experiment of Reference 1, the limiting value (extrema) of the axial component of the mean-flow Mach number would have been 1.0. This is the true (formal) quantitative definition of the limit-loading condition, which is reaching the extrema of the normal component of the mean-flow Mach

number. The figures presented in the previous section provide the qualitative (visual) evidence to support this hypothesis.

5.1 Axial-Flow Turbine Mean-Flow Mass Flux

The behavior of the mean-flow mass flux in an axial-flow turbine blade row, from subcritical, critical, and on to supercritical flow conditions, was also unexpected. Some analytical work suggests the mean-flow mass flux will increase up to the point of blade choking (critical condition) and then will remain as a constant thereafter (e.g., Ref. 5). Other work implies that the mean-flow mass flux will reach the critical value at blade choking and would then decrease in the supercritical flow regime following the behavior of the supersonic branch of the one-dimensional mass-flow function (e.g., Ref. 6).

From the CFD results of the present study, it appears the first suggestion of the above (Ref. 5) is the correct one for the staggered blade-row (channel-flow) geometry, where the sonic line sprung out from one corner of the blade end into the blade passage (Figure 7).

The CFD results on the behavior of the mean-flow mass flux collected at Line 2 (immediately downstream from the blade-row discharge) from the 14 operating PRs studied is presented next, followed by some analysis. The mean-flow mass flux was processed and obtained formally from the CFD results using Equation (5).

In Figure 10, the first plot contains results from all three tiers of meshes. Large oscillatory behavior at the coarse mesh is seen, but as noted previously in Section 4.2, the magnitude of oscillation subsided when the mesh was refined. This suggests the oscillatory behavior is numerical in nature and may be further reduced with even higher-mesh density (Figure 10(b)).

At PR = 1.5, the flow is subcritical; at PR = 2.25, the flow is critical (onset of blade-choking); and at PR >2.25, the flows are supercritical (beyond choked) (Figure 10(c)). Apart from the oscillations, which made it difficult to be conclusive, the mean-flow mass flux shown here is increasing through the subcritical flow regime to the critical condition and does not appear to be decreasing thereafter. In fact, it could be hypothesized that the mean-flow mass flux is constant throughout the supercritical flow regime as that observed at the critical flow condition if the up and down oscillations exhibited in the plot of Figure 10(c) are asymptotically eliminated.

The reason for this behavior of the mean-flow mass flux is because flow at the blade-row discharge is deflected by an angle (in the tangential direction) at the critical condition and beyond (the supercritical flow conditions) (Ref. 5). This angle of deflection is directly related to the amount of flow mass-flux allowed through in the blade passage, in the way that the mean-flow mass flux will stay at a constant value at and beyond the critical flow condition. In Reference 5, this constant mass flow flux was assumed and applied as the critical value obtained from a one-dimensional mass flow function.

As observed in Figure 10 (developed from the data obtained in the CFD study), it appears that this rationale is correct. However, no definitive proof exists to explain this behavior. The constant mass-flux may be slightly different from the value obtained at the critical condition of this analytical one-dimensional mass flow function. However, from extensive tests performed with AXOD/AXOD2 (Refs. 7 and 8), which is the code that was developed based on the work of Reference 5, the results indicated the following:

(1) The mean-flow mass flux value remains constant in supercritical conditions.
(2) The mean-flow mass flux value equals the critical mean-flow mass flux of this one-dimensional mass flow function.

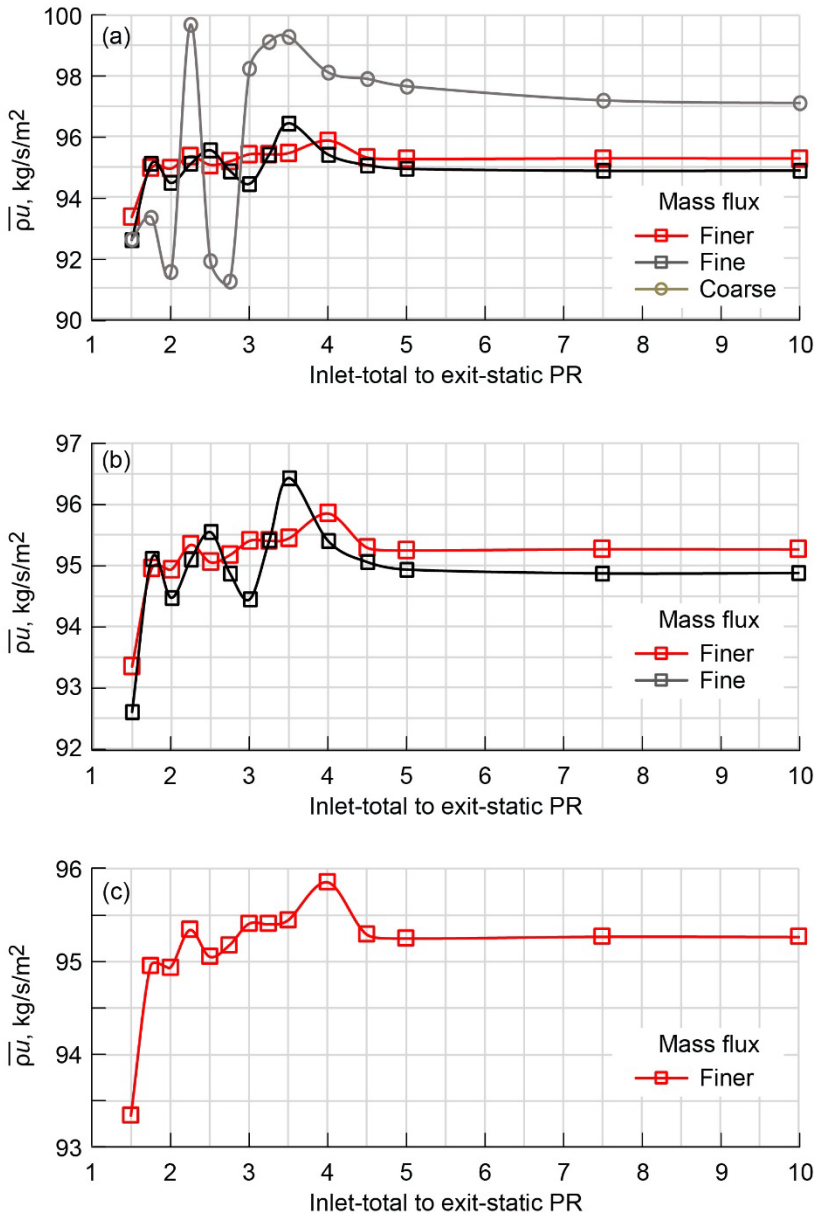

Figure 10.—Mean-flow mass flux. (a) Three tiers of mesh. (b) Fine and finer mesh. (c) Finer-mesh system. PR, pressure ratio.

The treatment in AXOD/AXOD2, in regard to the mean-flow mass flux and the behavior of the limit-loading condition in the supercritical flow regime described in this paper, is the subject of a follow-on paper (the Part II of this paper), to be published at a future date. The treatment applied in AXOD/AXOD2 on supercritical flows was mentioned in both References 1 and 2 as the most successful method among the five analytical methods that were compared.

The description presented in this paper holds true for axial-flow turbine blade rows in which the geometry at the blade-row discharge is predominantly a constant area or a slightly divergent, staggered channel-flow geometry. It would not be true for a geometrically prominent convergent-divergent channel (/nozzle), in which the suggestion made in Reference 6, that the flow rate would decrease as described by the supersonic branch of the one-dimensional mass flow function, would be truer. For an axial-flow turbine application of the aircraft engine, where the blade-row geometry at discharge has no, or has only a

negligible amount of geometrical divergence, the flow mass-flux and the flow angle at blade-row discharge, at supercritical flow condition, should consider the presence and the effect of supersonic flow deflection. However, the quantitative difference to the outcome of the two methods of approach cited here is in fact fairly small, as far as flows in the lower supercritical flow regime are concerned. This is evident from the plots and pictures presented in this paper. At low supersonic outflows, the streamlines are minimally deflected, and shown in Figure 3 at low supercritical conditions, for example PR < 3.0 (or more appropriately, Mach < 1.3 seen from the first plot of Figure 3), the discharge mean-flow angle deflection is in fact nearly the same as that of the critical flow condition (which has only about a 1° difference with respect to the subcritical flow conditions). Likewise, if examining the analytical one-dimensional mass flow function at low supersonic outflow, at Mach < 1.3 the mass flux on the supersonic branch of the flow function also remains close to the critical value, that is, the critical mass flux (the relation of this, actually is observable more directly and adequately from the plot of the discharge-flow angle deflection, displayed in Figure 3; since the discharge-flow angle deflection reflects directly to the relation of the mean-flow mass flux deviation, with respect to the critical flow mass flux). Therefore, although the methods of treatment in the supercritical flow regime are different between that of the Reference 5 and that of the Reference 6, but for low supercritical (low supersonic) outflows with Mach number no higher than 1.3 across the blade span, the quantitative difference of both the mean-flow angle at discharge and the mean-flow mass flux between the two approaches would be small, to apply as preliminary design-analysis for axial-flow turbine as an acceptable practice, when the design requirement dictates that the design point (or the design outcome) is to occur in the supercritical flow regime (the overall discharge-flow angle across the blade span would differ by about 1°, while the overall flow rate would have nearly no difference, between the two methods).

A form of this analytical one-dimensional mass-flow function is given here by Equation (9). This equation, in various forms, can be found in References 2 and 4

$$\left(\frac{\omega}{A}\right)*\frac{\sqrt{Tt}}{Pt}=\mathrm{M}\sqrt{\frac{\gamma G}{R}}*\sqrt{\frac{Tt}{T}}*\left(\frac{Pt}{P}\right)^{-1} \tag{9}$$

where
A is a cross section area normal to the flow
G is a unit conversion factor needed for the system of U.S customary units
P is the static pressure
Pt is the total pressure
R is the specific gas constant
T is the static temperature
Tt is the total temperature
γ is the specific heat ratio
ω is the mass flow rate

5.2 Total-Pressure-Loss Coefficients

The total pressure loss in a turbine through flow is the foundation of all predictive methods used in the turbine field for design and/or analysis. A total-pressure-loss coefficient is defined in Equation (7) and calculated from the CFD results obtained in this study. The total-pressure-loss coefficients obtained at Lines 1 and 2 were plotted and are presented here (Figure 11). The Line 2 (immediately downstream from the rotor) result is presented first, followed by the result at Line 1 (near the exit plane).

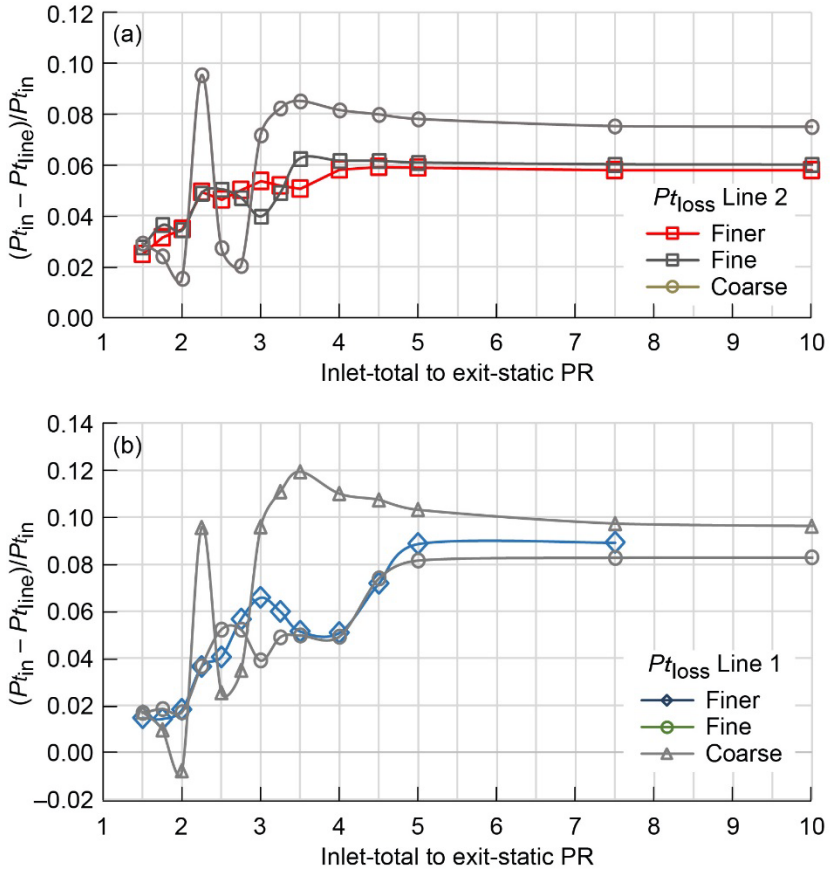

Figure 11.—Total-pressure-loss coefficients. (a) Line 2. (b) Line 1. PR, pressure ratio.

As shown in Figure 11, the total pressure loss at Line 1 is somewhat lower than that at Line 2 in the subcritical flow regime, indicating that diffusion and kinetic energy dissipation are the dominant factors downstream from the blade-row discharge in subsonic outflows. The loss at Line 1 is noticeably higher than that of Line 2 in the supercritical flow regime, suggesting that the characteristic wave interaction with the flow is the dominant effect in supersonic outflows. The result at PR = 10.0 was not included in the finer-mesh plot of Line 1 due to the data contamination cited in Section 4.4.4.

Total pressure loss is positive for all turbine flows, subcritical to supercritical, in the finer-mesh results. Apart from the wavy behavior, which could be for real in total-pressure-loss coefficients (structure-wise it is fairly smooth), the total pressure loss is increasing in the supercritical flow regime (PR > 2.25) when compared with the loss in the subcritical flow regime (PR < 2.25). This suggests that the loss model that was developed based on correlations of the subcritical flows (lower PRs, unchoked condition) would have to be corrected in the supercritical flow regime (at beyond-choke operations). In Reference 7, a third-order polynomial correction function was suggested and implemented in AXOD from a designated starting PR (PR = 2.0) to a designated ending PR (representing the point of establishment of the limit-loading condition, e.g., PR = 5.0 of this study). Currently, however, a simple monotonic decrease with a linear function is applied to the baseline blade-row efficiency model in AXOD2 as an extra blade-row efficiency reduction to mimic this increased loss. This seems to have yielded comparatively good results and behavior for flows in the supercritical flow regime. More on this will be addressed in Part II of the paper.

6.0 Concluding Remarks

A CFD (computational fluid dynamics) investigation was conducted over a two-dimensional axial-flow turbine rotor blade row to study the phenomena of turbine rotor discharge-flow overexpansion at subcritical, critical, and supercritical conditions. The computational bases and rationale are the same as those applied and executed in the experiment of Hauser, Cavour H.; Plohr, Henry W.; and Sonder, G.: Study of Flow Conditions and Deflection Angle at Exit of Two-Dimensional Cascade of Turbine Rotor Blades at Critical and Supercritical Pressure Ratios. NACA RM E9K25, 1950. http://ntrs.nasa.gov, on the same subject, but with a different rotor blade shape. Quantitative data of the mean-flow Mach numbers, mean-flow angles, the tangential-blade surface-pressure forces, the mean-flow mass flux, and the flow path total-pressure-loss coefficients, averaged across the two-dimensional computational domain encompassing two blade passages, were obtained over a series of 14 inlet-total to exit-static PRs, from 1.5 (unchoked; subcritical condition) to 10.0 (supercritical with excessively high PR). Detailed flow features over the full domain of computation, such as the streamline patterns, Mach contours, pressure contours, blade surface pressure distributions, and so forth, were collected and presented in this paper. A formal, quantitative definition of the limit-loading condition based on the channel flow theory was proposed and explained.

Appendix A.—Blade Surface Static Pressure Distribution

No flow separation was detected in any of the 14 ratios studied. The wall shear stresses were positive all around the blade over the entire length.

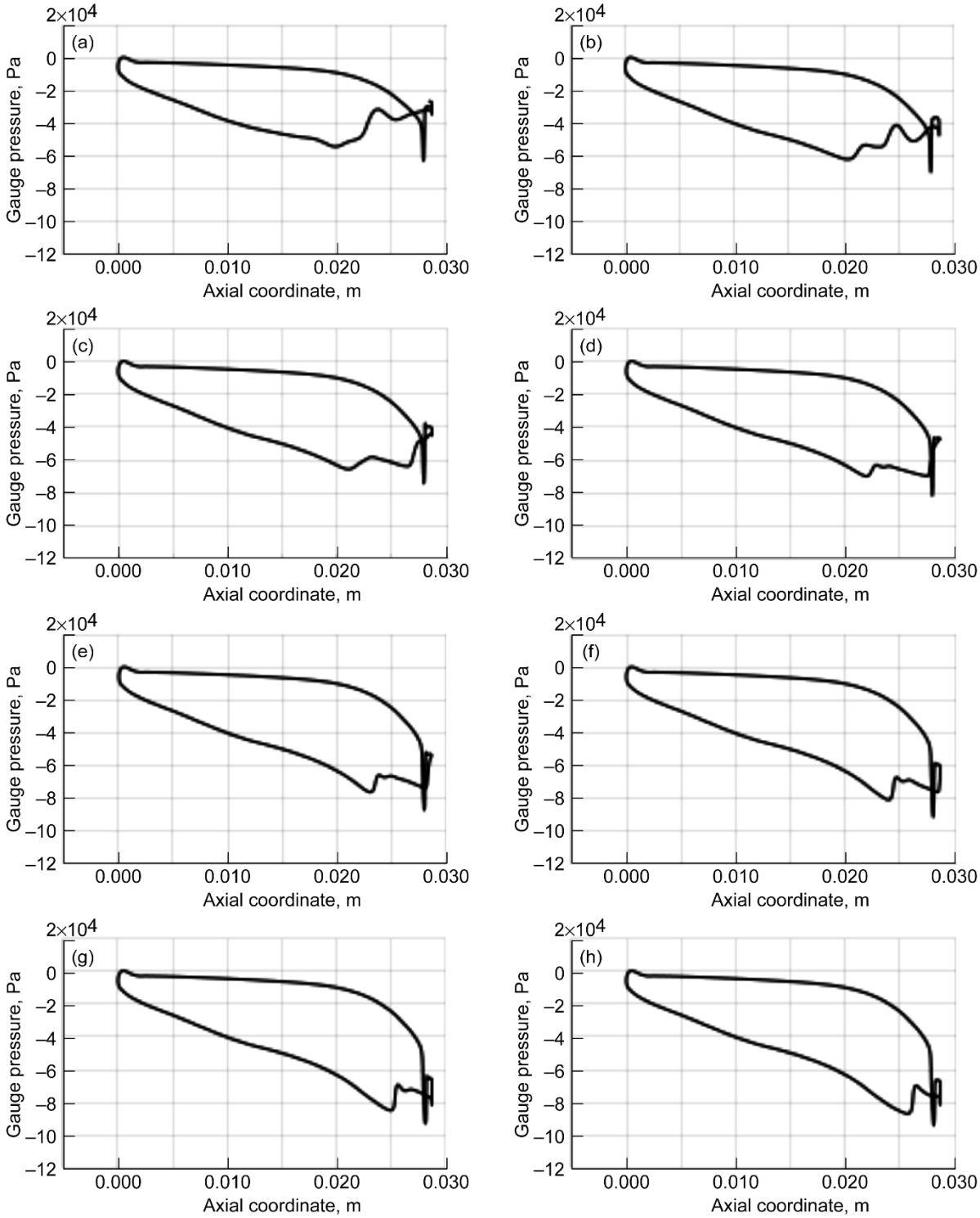

Figure A.1.—Blade surface static pressure. (a) Pressure ratio (PR) = 1.5. (b) PR = 1.75. (c) PR = 2.0. (d) PR = 2.25. (e) PR = 2.5. (f) PR = 2.75. (g) PR = 3.0. (h) PR = 3.25.

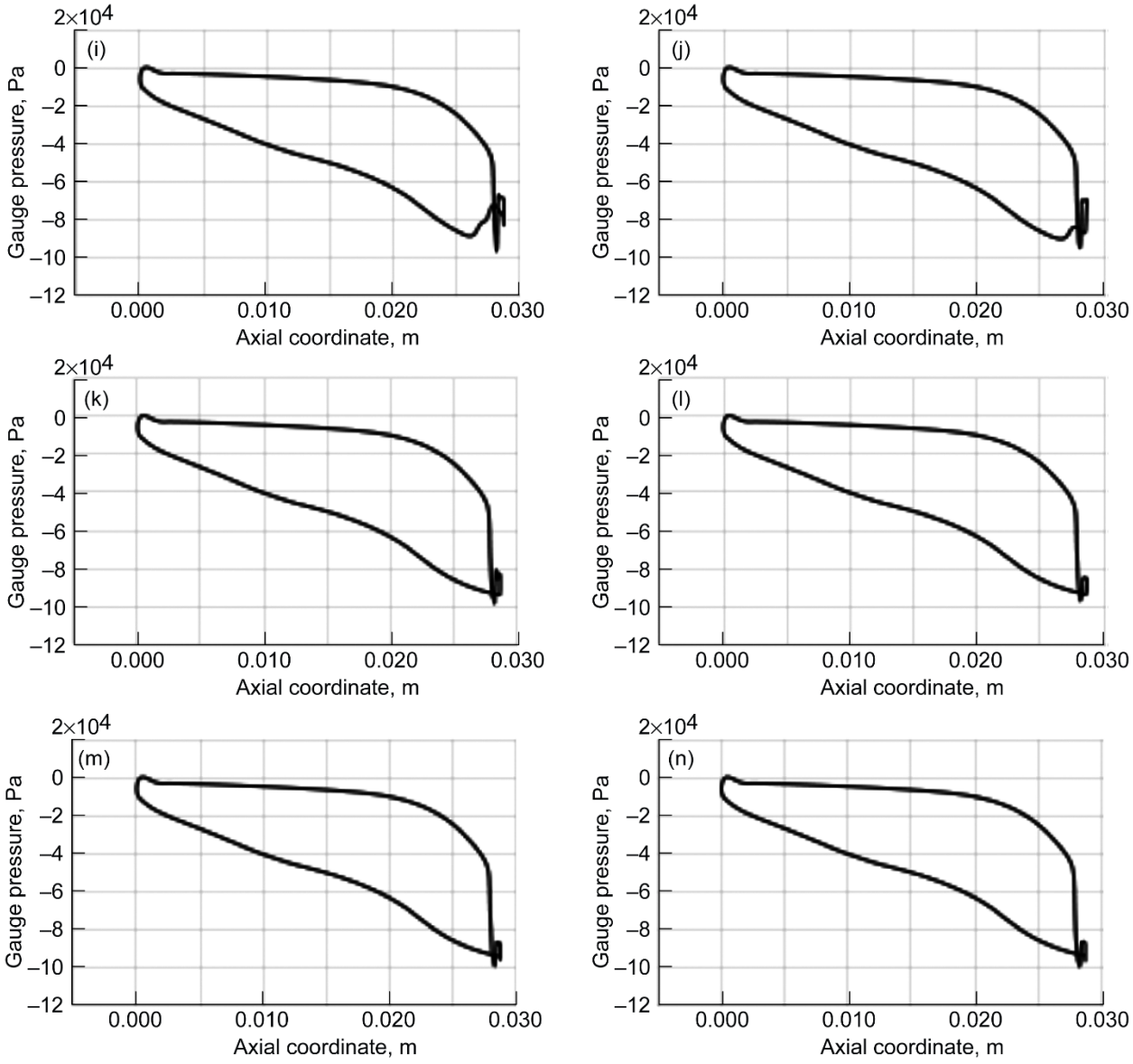

Figure A.1—.Concluded. (i) Pressure ratio (PR) = 3.5. (j) PR = 4.0. (k) PR = 4.5. (l) PR = 5.0. (m) PR = 7.5. (n) PR = 10.0.

Appendix B.—Flow Features and Patterns of Remaining Ratios Investigated

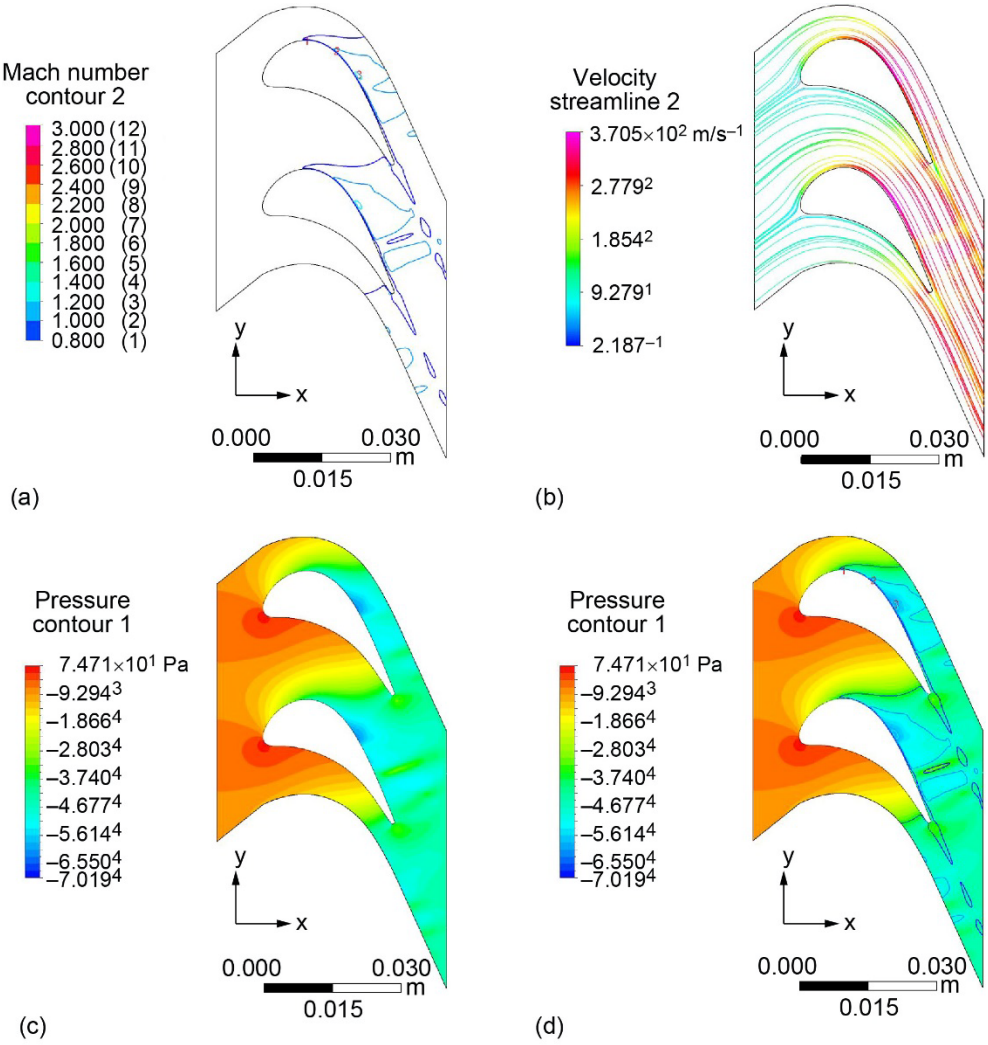

Figure B.1.—Flow pattern and streamline contour, where subcritical flow at pressure ratio (PR) = 1.75. (a) Mach contour. (b) Streamlines. (c) Pressure contour. (d) Pressure with Mach contour imposed.

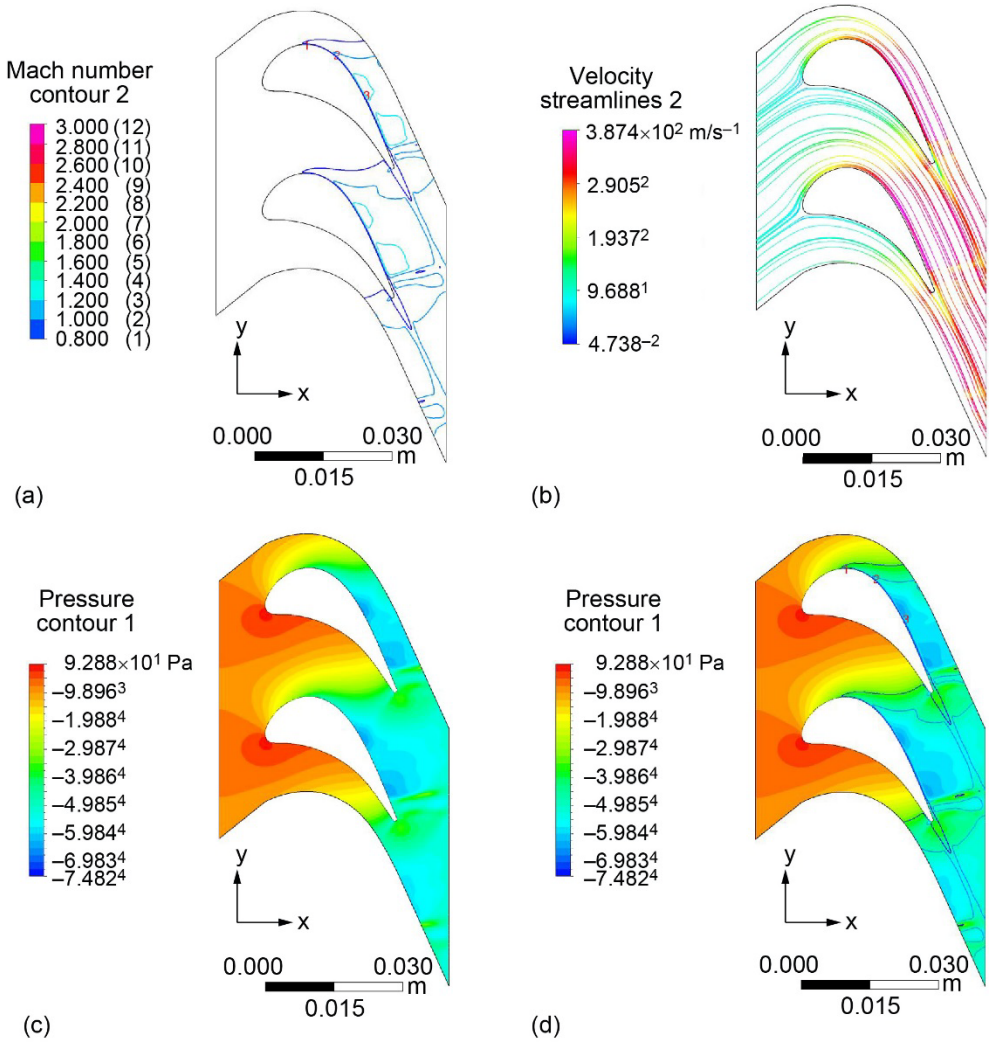

Figure B.2.—Flow pattern and streamline contour, where subcritical flow at pressure ratio (PR) = 2.0. (a) Mach contour. (b) Streamlines. (c) Pressure contour. (d) Pressure with Mach contour imposed.

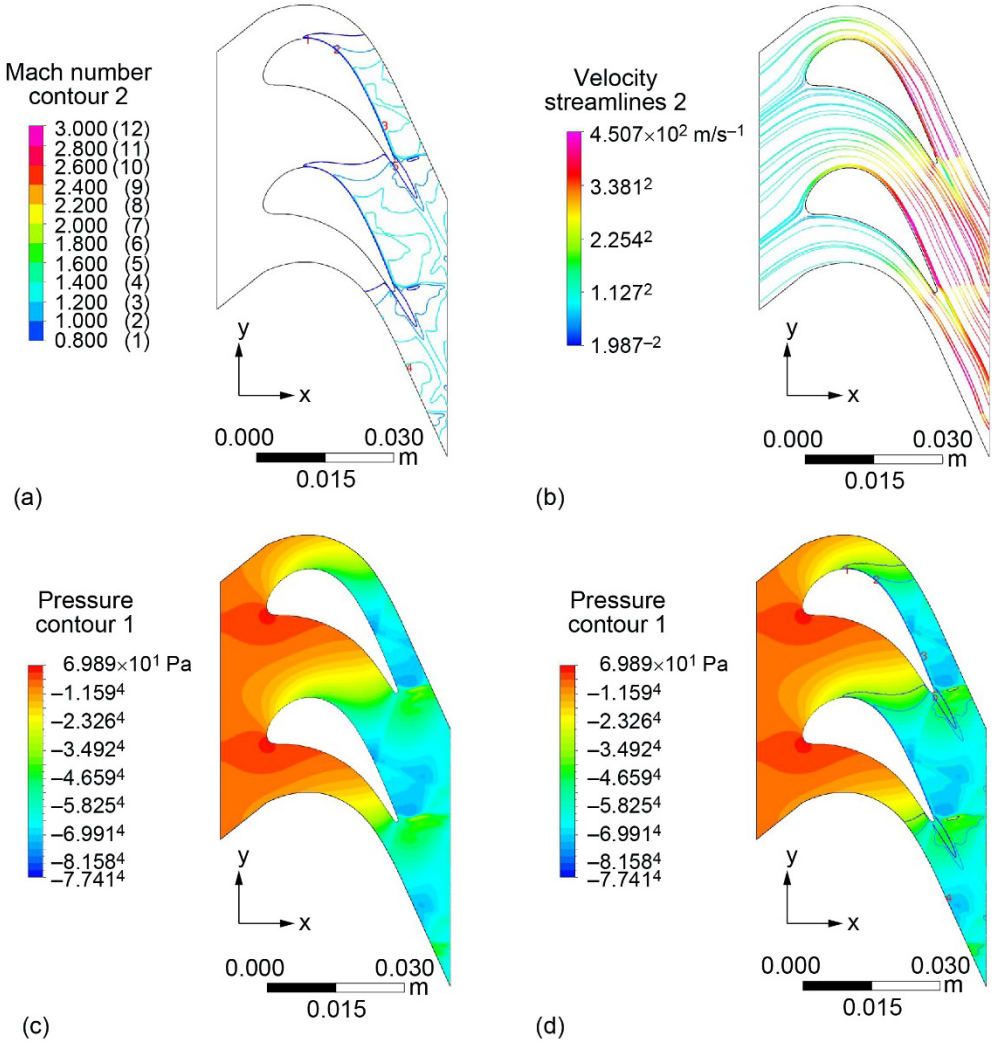

Figure B.3.—Flow pattern and streamline contour, where supercritical flow at pressure ratio (PR) = 2.5. (a) Mach contour. (b) Streamlines. (c) Pressure contour. (d) Pressure with Mach contour imposed.

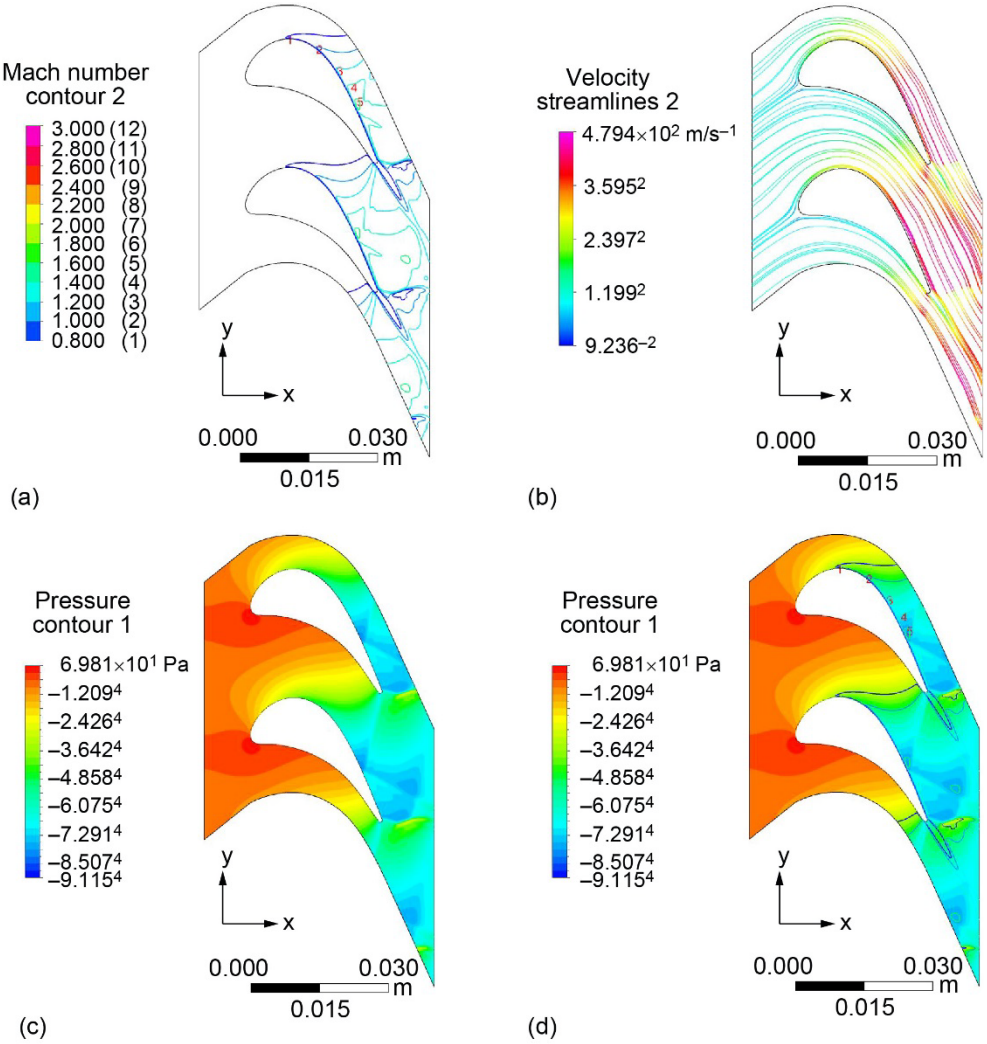

Figure B.4.—Flow pattern and streamline contour, where supercritical flow at pressure ratio (PR) = 2.75. (a) Mach contour. (b) Streamlines. (c) Pressure contour. (d) Pressure with Mach contour imposed.

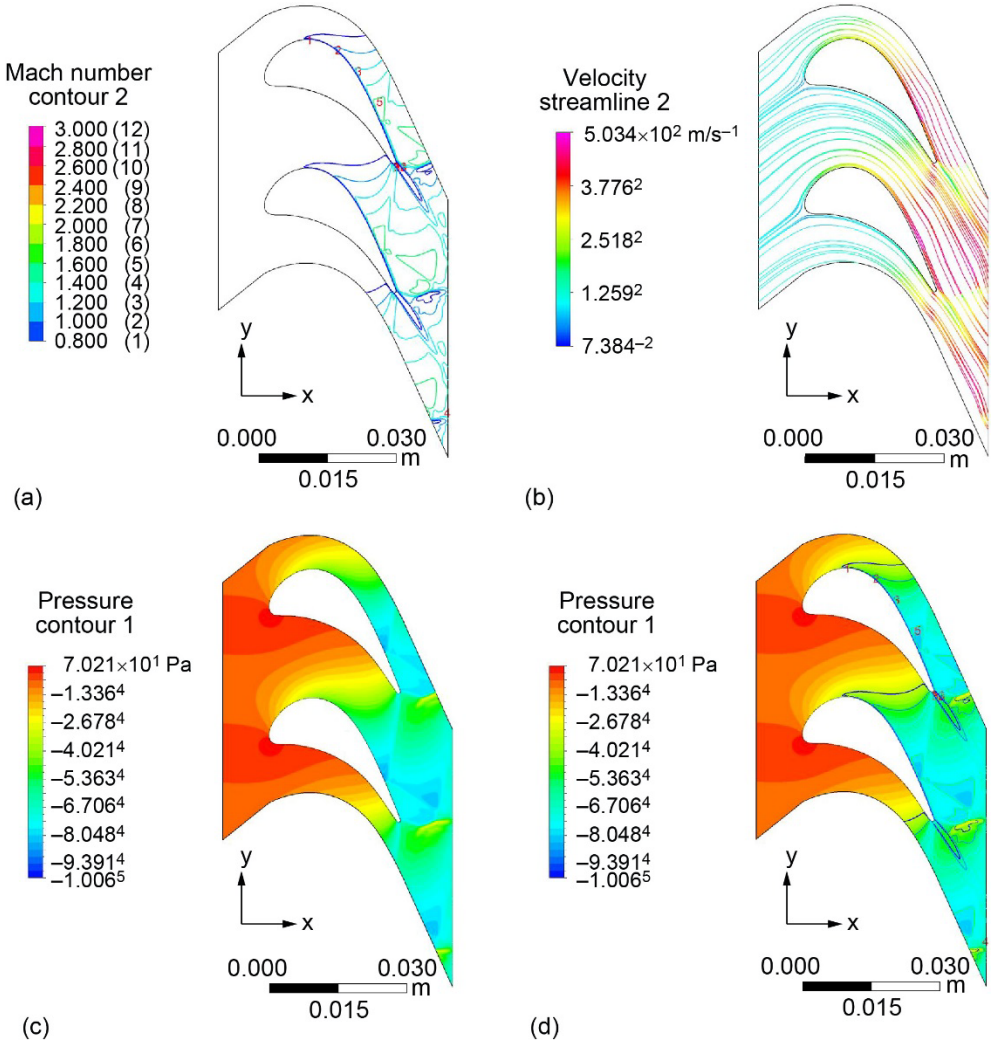

Figure B.5.—Flow pattern and streamline contour, where supercritical flow at pressure ratio (PR) = 3.0. (a) Mach contour. (b) Streamlines. (c) Pressure contour. (d) Pressure with Mach contour imposed.

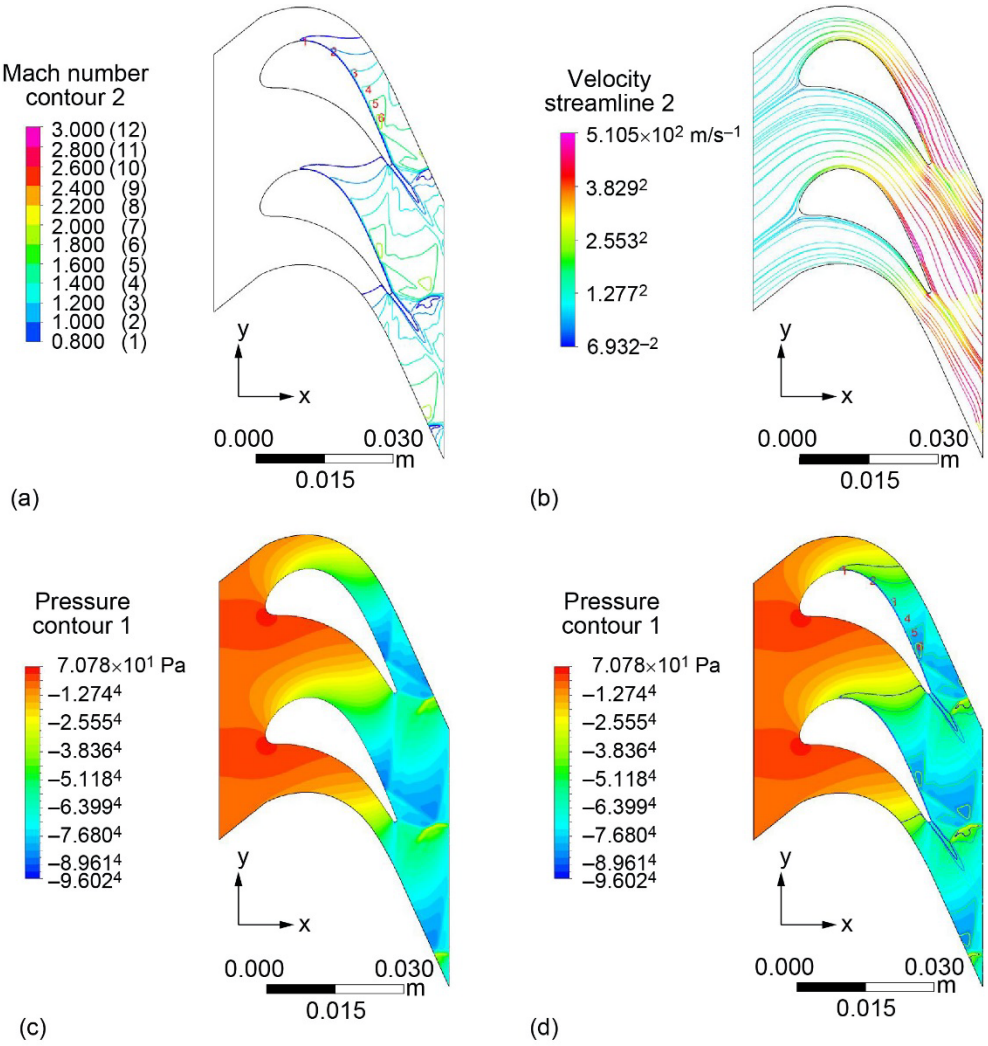

Figure B.6.—Flow pattern and streamline contour, where supercritical flow at pressure ratio (PR) = 3.25. (a) Mach contour. (b) Streamlines. (c) Pressure contour. (d) Pressure with Mach contour imposed.

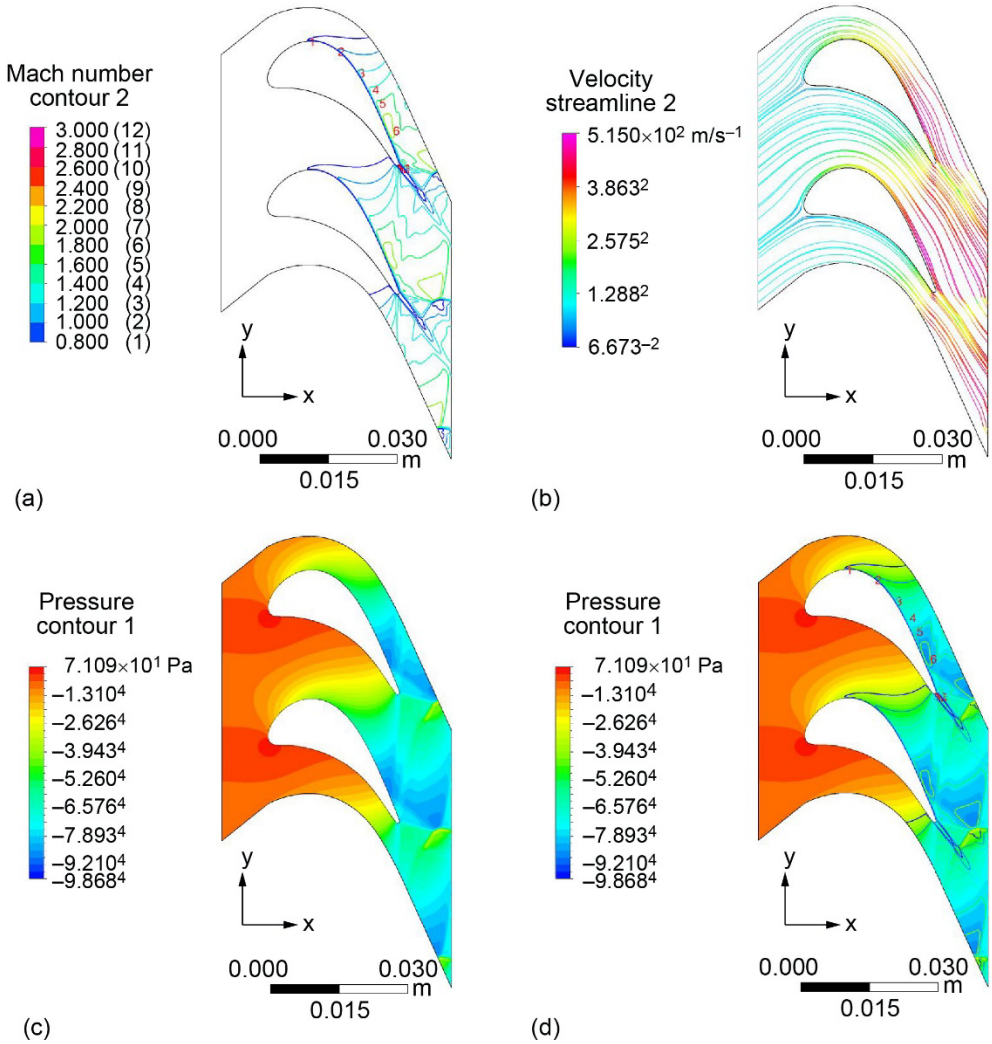

Figure B.7.—Flow pattern and streamline contour, where supercritical flow at pressure ratio (PR) = 3.5. (a) Mach contour. (b) Streamlines. (c) Pressure contour. (d) Pressure with Mach contour imposed.

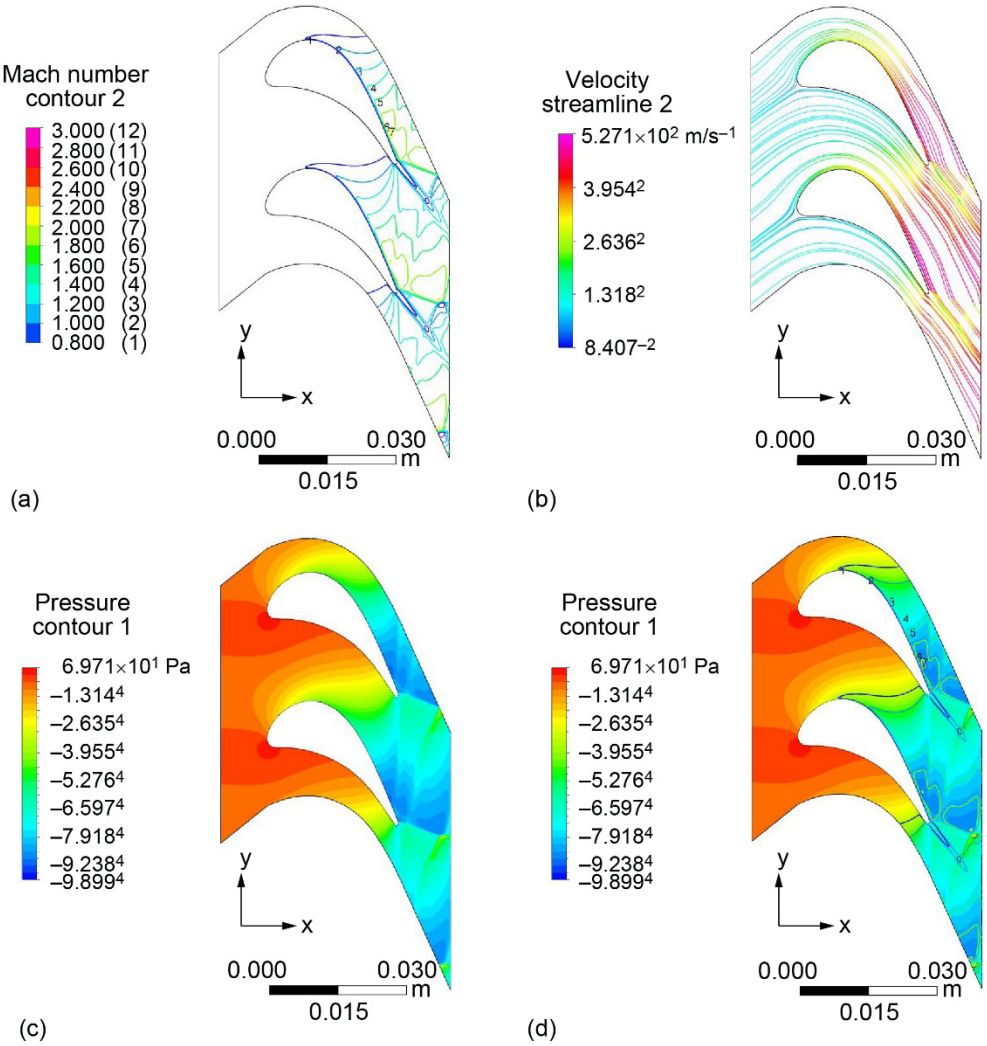

Figure B.8.—Flow pattern and streamline contour, where supercritical flow at pressure ratio (PR) = 4.0. (a) Mach contour. (b) Streamlines. (c) Pressure contour. (d) Pressure with Mach contour imposed.

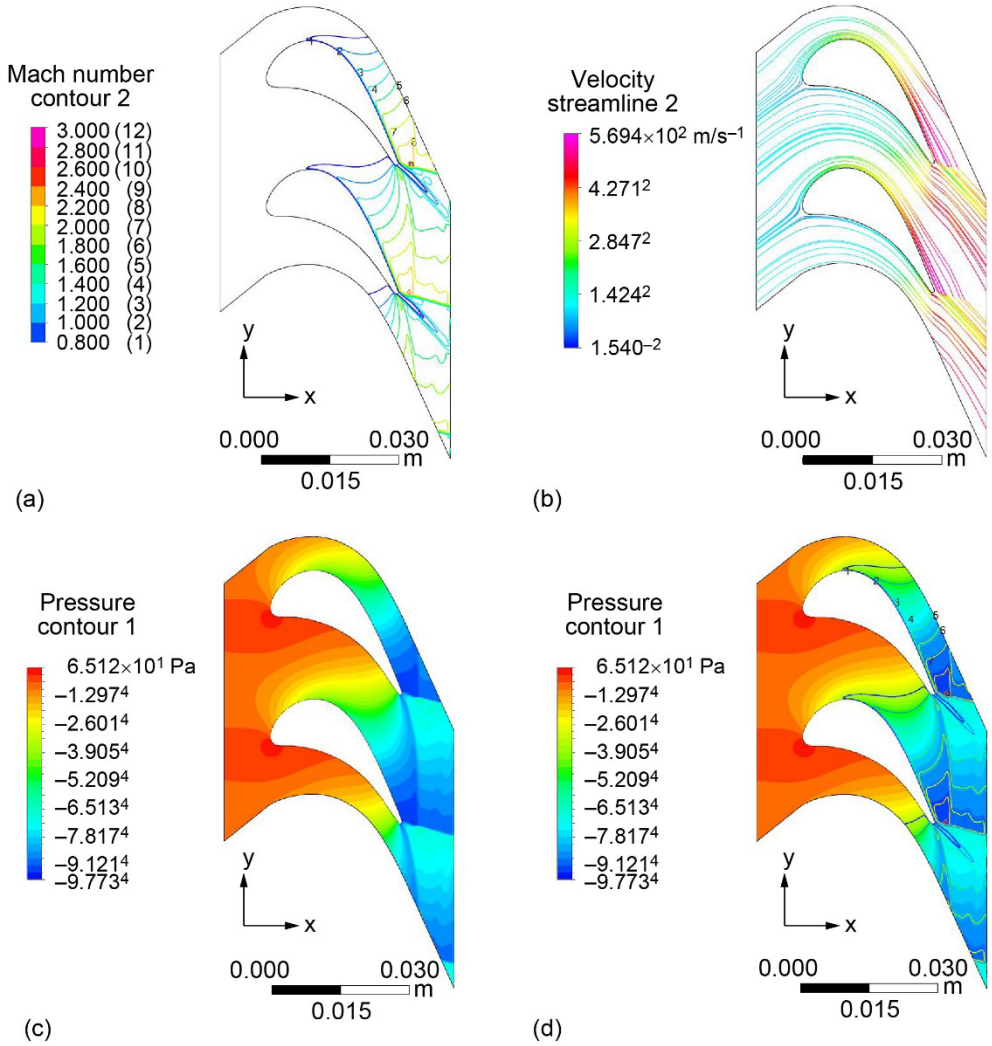

Figure B.9.—Flow pattern and streamline contour, where supercritical flow at pressure ratio (PR) = 5.0. (a) Mach contour. (b) Streamlines. (c) Pressure contour. (d) Pressure with Mach contour imposed.

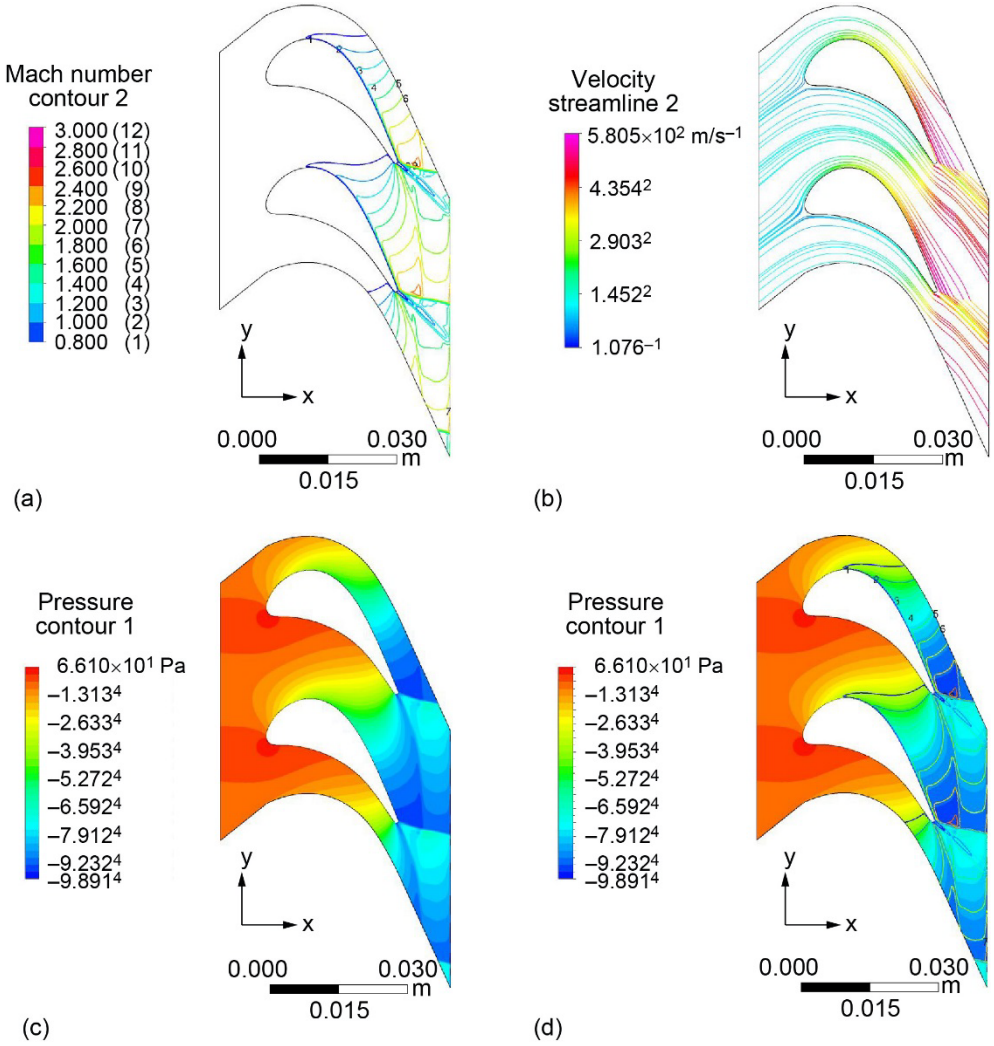

Figure B.10.—Flow pattern and streamline contour, where supercritical flow at pressure ratio (PR) = 7.5. (a) Mach contour. (b) Streamlines. (c) Pressure contour. (d) Pressure with Mach contour imposed.

References

1. Hauser, Cavour H.; Plohr, Henry W.; and Sonder, G.: Study of Flow Conditions and Deflection Angle at Exit of Two-Dimensional Cascade of Turbine Rotor Blades at Critical and Supercritical Pressure Ratios. NACA RM E9K25, 1950. http://ntrs.nasa.gov
2. Horlock, J.H.: Axial Flow Turbines: Fluid Mechanics and Thermodynamics. Robert E. Krieger Publishing Co., Malabar, FL, 1982.
3. Timko, L.P.: Energy Efficient Engine High Pressure Turbine Component Test Performance Report. NASA CR–168289, 1990. http://ntrs.nasa.gov
4. Shapiro, Ascher H.: Compressible Fluid Flow. Vol. 1, John Wiley & Sons, Inc., New York, NY, 1953.
5. Flagg, E.E.: Analytical Procedure and Computer Program for Determining the Off-Design Performance of Axial Flow Turbines. NASA CR–710, 1967. http://ntrs.nasa.gov
6. Carter, A.F.; Platt, M.; and Lenherr, F.K.: Analysis of Geometry and Design Point Performance of Axial Flow Turbines, I—Development of the Analysis Method and the Loss Coefficient Correlation. NASA CR–1181, 1968. http://ntrs.nasa.gov
7. Glassman, Arthur J.: Modeling Improvements and Users Manual for Axial-Flow Turbine Off-Design Computer Code AXOD. NASA CR–195370, 1994. http://ntrs.nasa.gov
8. Chen, Shu-Cheng S.: A Guide to Axial-Flow Turbine Off-Design Computer Program AXOD2. NASA/TM—2014-218301, 2014. http://ntrs.nasa.gov